Modeling the effects of surface plasmon resonance on hot electron collection in a metallic-semiconductor photonic crystal device

by

Xinhao Li

Submitted to the Department of Mechanical Engineering in partial fulfillment of the requirements for the degree of Master of Science in Mechanical Engineering

at the

MASSACHUSETTS INSTITUTE OF TECHNOLOGY

June 2017

Author ..... Signature redacted

Department of Mechanical Engineering

May 10, 2017

Certified by ..... Signature redacted .....

Prof. Sang-Gook Kim

Professor of Mechanical Engineering

Thesis Supervisor

Accepted by ..... Signature redacted

Prof. Rohan Abeyaratne

Quentin Berg Professor of Mechanics

Chari, Committee of Graduate Students

Modeling the effects of surface plasmon resonance on hot electron collection in a metallic-semiconductor photonic crystal device

by

Xinhao Li

Submitted to the Department of Mechanical Engineering

On May 10, 2017, in partial fulfillment of

the requirements for the degree of

Master of Science in Mechanical Engineering

Abstract

Metallic-semiconductor Schottky hot carrier devices have been found as a promising solution to harvest photon with energy below the bandgap of semiconductor, which is of crucial importance for realizing efficient solar energy conversion. In recent years, extensive efforts have been devoted to utilizing surface plasmon resonance to improve light absorption by creating strong light-metal interaction, which generates hot electrons through non-radiative decay. However, how surface plasmon enhances the efficiency of hot electron collection is still debatable.

This thesis studies the effects of surface plasmon resonance on hot electron collection in a metallic-semiconductor photonic crystal (MSPhC) designed by our group for efficient photoelectron-chemical energy conversion. In contrast to a broadband light absorption at the range from 400 nm to 800 nm, the sub-bandgap photoresponse shows a single peak centered at 590 nm, which is identified as the surface plasmon resonant wavelength of this device. We develop a theoretical model of hot electron generation, transport and injection in this device incorporating the effects of anisotropic hot electron momentum distribution caused by surface plasmon resonance. Near resonant wavelength, surface plasmon dominates the electric field in the thin Au layer, which generates hot electrons with high enough momentum preferentially normal to the Schottky interface. Through analyzing the energy, momentum and spatial distribution of generated hot electrons, we develop a model to estimate the internal quantum efficiency (IQE) of this device. The anisotropic hot electron momentum distribution largely enhances IQE and photoresponse near the resonant wavelength. Compared with the widely used Fowler's theory of Schottky internal photoemission, our model can better predict IQE of surface plasmon assisted hot electron collection. Combined with large scale photonic design tools, this quantum-level model could be applied for tuning and enhancing photoresponse of Schottky hot carrier devices.

Thesis Supervisor: Sang-Gook Kim
Title: Professor of Mechanical Engineering

Acknowledgments

Foremost, I would like to thank my thesis advisor, Prof. Sang-Gook Kim, for his support of my study and research, and patient guidance of the direction of the project. This thesis work would not be possible without his inspiration and advice. Secondly, I would like to thank Dr. Jeffrey Chou and Ms. Yu Wang, from whom I took over this project. They designed the device architecture and fabricated the first batch of MSPhC, which is the foundation of this work. Thank you for leading me into the project and helping me with many technical problems. I would also like to thank Prof. Jaime Viegas and Prof. Mustapha Jouiad and their groups at Masdar Institute of Science and Technology for providing helps on material characterization and surface plasmon investigation. Their excellent work using Electron Energy Loss Spectroscopy provided deep insights in understanding the surface plasmon resonance in MSPhC. I would also like to thank Prof. Wei Lek Kwan who provided suggestions on the theoretical modeling of internal photoemission. I would also like to thank my labmates, Mr. Ruize Xu, Dr. Katherine Smyth and Mr. Haluk Akay for their generous help.

Finally, I want to express my gratitude and appreciation to my family for their support and love, and many friends who helped me throughout challenges in my research and life.

Contents

List of figures

List of tables

Chapter 1. Introduction

1.1 Hot carrier collection for reducing sub-bandgap energy loss

The fundamental limitation on solar energy conversion efficiency by photovoltaic and photoelectron-chemical devices, which use semiconductors is the absorption threshold at the bandgap of semiconductor [1, 2]. As shown in Fig. 1.1 (a), photon with energy lower than the bandgap cannot be harvested for energy conversion, which significantly reduces the efficiencies of applications such as solar cells and photocatalytic devices. For example, rutile and anatase TiO_2, which have been widely used as a stable semiconductor catalyst for solar water splitting, have bandgap of about 3.0 eV and 3.2 eV [3]. This large bandgap severely restricts solar-to-fuel conversion efficiency since the sub-bandgap energy loss at visible spectrum.

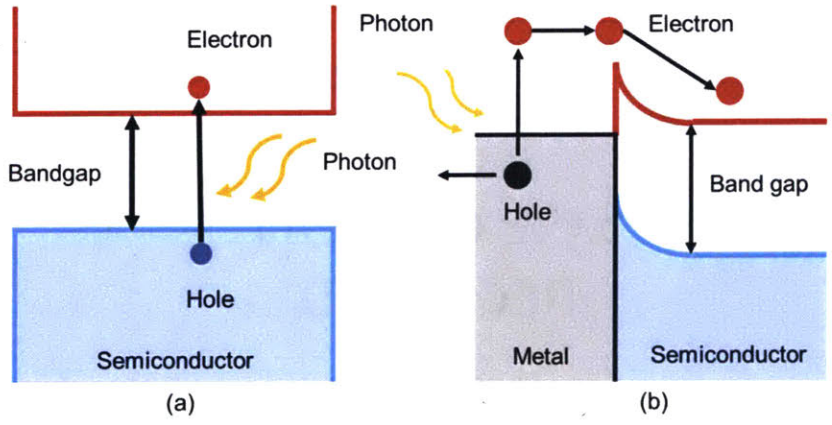

Figure 1.1 Schematic of photoelectric energy harvesting in (a) semiconductors with large bandgaps and (b) metallic-semiconductor Schottky junctions.

Adding a second material layer of metal can form Schottky junction at the interface between metal and semiconductor, which provides a promising solution to enhance the

photoelectric energy harvesting at sub-bandgap spectrum [4]. Electrons in metal could be excited by absorbing photons to the energy level higher than the thermal distribution, which is the so called "hot electrons" [5]. Depending on the band diagram of Schottky junction, hot electrons with energy higher than the barrier can be injected on to the conduction band of semiconductor, as shown in Fig. 1.1 (b). When the barrier height is lower than the bandgap of semiconductor, metallic-semiconductor Schottky hot carrier device provides a promising solution to harvest sub-bandgap solar energy [6].

$$I(v) = A(v) \cdot \eta_{IQE}(v) \cdot \frac{q}{hv} \tag{1.1}$$

The photoresponse of an photoelectric device equals absorption times the internal photoemission efficiency [4], as shown in Eq. (1.1), where I is photoresponse, A is absorption, η_{IQE} is internal quantum efficiency (IQE), q is unit electron charge, v is frequency and h is Planck's constant. In order to extend and enhance the sub-bandgap photoresponse spectrum, we need to improve the absorption by metal in the Schottky hot carrier device. Recently, our group reported a two dimensional metallic dielectric photonic crystal (MDPhC), which achieves selective broadband absorption of sunlight at the range from visible to near-IR [7, 8]. By supporting high density cavity modes in the structure of nano-cavity array, the light-matter interaction time can be largely increased, which improves absorption. Inspired by MDPhC, we designed a metallic-semiconductor photonic crystal (MSPhC) device with two dimensional nano-cavity array to increase light absorption by metal material [9]. By coupling light into cavity, waveguide and surface plasmon resonance modes in the structure, absorption is

significantly enhanced in the visible range. In Section 1.2, we will review the design of this device by Finite-Difference Time-Domain (FDTD) simulation method.

On the other hand, the improvement of internal photoemission efficiency relies on understanding the hot electron's generation, transfer and injection process [10]. The Fowler's theory have been widely used in modeling the internal photoemission between metal and semiconductor, which is based on free-electron like Jellium model as band structure for metal and only considers the electron's intraband transition [11, 12]. Besides, it assumes that the generated hot electrons distribute isotopically and uniformly in the momentum space. The so called "Escape Cone" model is used as criteria for hot electron injection in Fowler's theory, in which only electrons with enough energy component perpendicular to the metal-semiconductor interface could be injected. With all of the above assumptions, the IQE of a Schottky device could be fitted to the Fowler's equation [4, 11]:

$$\eta_{IQE}(v) = C \cdot \frac{(hv - q\phi_B)^2}{hv \cdot q\phi_B} \tag{1.2}$$

ϕ_B is the height of Schottky barrier and C is a fitting constant. Recent experimental results have shown that in some devices with surface plasmon resonance, the applicability of Fowler's theory is limited [13-15]. In Section 1.3 we will introduce the concept of surface plasmon and its application in solar energy harvesting, while in Section 1.4 we will review previous results in modeling plasmon assisted hot carrier collection.

1.2 Device design and fabrication of MSPhC

Inspired by MDPhC, we designed the MSPhC with two dimensional nano-cavity array. Figure 1.2 (a) shows the top view of a 1 cm by 1cm MSPhC chip. Multiple layers are deposited on the Al_2O_3 nano-cavity arrays we fabricated for solar absorbers before [7, 8]. 200 nm Au and Ti layer are used as probe contact at the two ends of the chip. The widths of region I, III and IV are approximately 2 mm. Figure 1.2 (b) shows the basic structure and operation design of MSPhC of the II and III region in Fig. 1.2 (a), which uses a thin Au layer as the optical absorber, TiO_2 as the n-type semiconductor layer, and indium tin oxide (ITO) as the back transparent electrical contact to reduce the series resistance. Au and TiO_2 are chosen due to their chemical stability and wide application in photoelectron-chemical devices [13]. As shown in Fig. 1.2 (c), the cavity structure could support three light absorption modes: cavity, waveguide and surface plasmon modes. These modes increase the total light absorption of the device by increasing the light-matter interaction time, especially in the Au layer. Figures 1.2 (d) and 1.2 (e) show the typical current path through Au/TiO_2/ITO interfaces and band diagram, and how hot electrons are generated and collected. After being excited at or below the Fermi level, hot electrons with enough energy could transfer through the interface between Au and TiO_2, be injected to and collected at the conduction band of TiO_2. Since the Schottky barrier height between Au and TiO_2 is typically 1.0 eV [6, 16], MSPhC device has the potential to harvest solar energy below the bandgap of TiO_2.

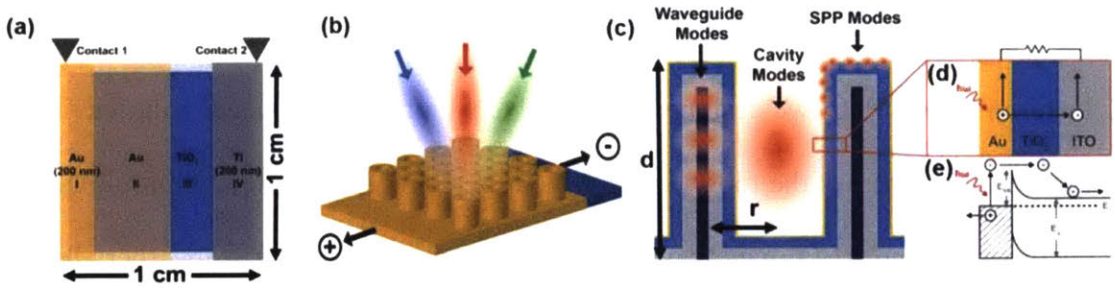

Figure 1.2 Schematic of MSPhC device. (a) Top view of MSPhC chip. Thick metal (200 nm) are used as contacts in region I and IV. (b) Structure and operation design of region II and III in (a). (c) Cross-section of MSPhC and possible resonance modes. r and d are the radius and depth of the nano-cavity. (d) Layer structure and current path. (e) Band diagram of Au/TiO_2 interface.

In order to improve the absorption by the thin Au layer, we used FDTD (Lumerical package) to find the optimized structure dimension and thickness of different material layers [9]. Generally, the trade-off between light-trapping ability and numbers of supported optical resonance modes determines the absorption of MSPhC. The absorption is largely determined by the cut-off frequency of cavity modes [8]. A larger and deeper cavity can support more modes, with a smaller cut-off frequency, at the cost of losing the confinement of incident light inside the structure. We varied the radius of cavity from 167 nm to 1,000 nm and depth from 250 nm to 1,500 nm, with thickness of different material layers as: 13 nm Au, 75 nm TiO_2, 50 nm Al_2O_3 and 30 nm ITO. FDTD simulation results show that the maximum total absorption of MSPhC happens when radius is 250 nm and depth is 1 μm for solar-weighted absorption. Besides, in order to increase the absorption by Au layer, the dependence of absorption by MSPhC on the thickness of Au layer has been studied by FDTD simulation. Thin layer of Au and the Al_2O_3 nano-cavity structure could allow the light to penetrate and couple with the

metal/insulator/metal (M/I/M) structure, which increases the light-metal interaction time and total absorption. Since the imaginary part of permittivity of Al_2O_3, TiO_2 are much smaller compared with Au below the bandgap of TiO_2, the thin gold layer contributes to most of the absorption at visible light range from 400 nm to 800 nm [17]. As shown in Fig. 1.3, in a nano-cavity structure with depth of 1 μm and radius of 250 nm, the absorption spectra extends from the cut-off wavelength of 740 nm to about 1,500 nm by reducing the thickness of the Au layer.

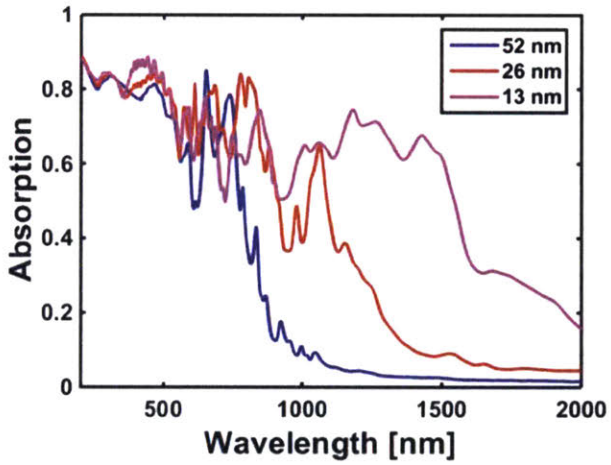

Figure 1.3 FDTD simulated absorption spectra of MSPhC with various Au thickness of 13 nm, 26 nm and 52 nm.

Through FDTD simulation, we also observed three possible kinds of optical resonance modes that could be supported in the nano-cavity structure, which are the cavity, waveguide and surface plasmon resonance modes. These different modes of absorption trap light inside MSPhC and improve the total absorption. By randomly distributing 9 broadband dipole sources inside the cavity structure, we intended to stimulate all of the possible resonance modes [9]. Figure 1.4 shows the intensity profile

of electric field at the cross-section of the nano-cavity at 500 nm, 600 nm and 750 nm, which are corresponding to waveguide mode in the M/I/M structure, surface plasmon resonance at the interface between Au and TiO_2 along the side wall and cavity mode inside the structure, respectively. Among these three modes, cavity and waveguide modes are low-loss modes since light is concentrated inside the cavity and Al_2O_3 side wall. On the other hand, surface plasmon resonance at the interface is high-loss mode, in which plasmons could decay non-radiatively by generating electron-hole pairs [5, 6, 18].

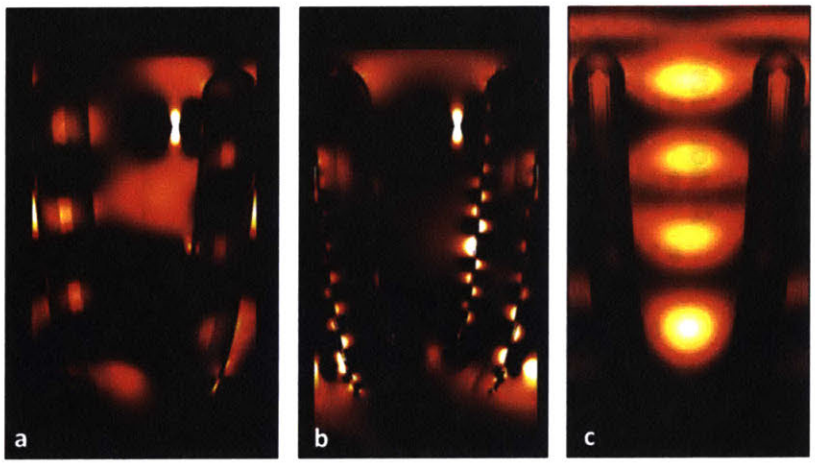

Figure 1.4 Intensity profile of electric field at cross-section of MSPhC at (a) 500 nm, (b) 600 nm and (c) 750 nm, which represent waveguide, surface plasmon resonance and cavity modes in the nano-cavity structure.

Through FDTD simulation, we found the optimized structure dimension to improve light absorption. The final structure we used in fabricating the device with highest photoresponse is as follows. The nano-cavity array of Al_2O_3 with depth of 1 μm, inner radius of 250 nm and distance between centers of two nearest cavities of 840 nm was patterned by basic side-wall lithography method on 6 inch silicon wafer. The detailed

fabrication process is shown in Fig. 1.5 (a), and in our previous published work [9, 19]. Then, thin layers of 30 nm ITO, 60 nm TiO_2 and 20 nm Au were deposited on Al_2O_3 nano-cavity arrays, followed with post annealing, as shown in Fig. 1.5 (b). Besides, in order to improve the diode performance of the Schottky junction, an ultra-thin layer of Al_2O_3 layer was deposited between TiO_2 and Au to reduce interfacial defect states [20]. Finally, 200 nm of Au and Ti layers were sputtered onto the two ends of each MSPhC chip as electrical contacts for device test.

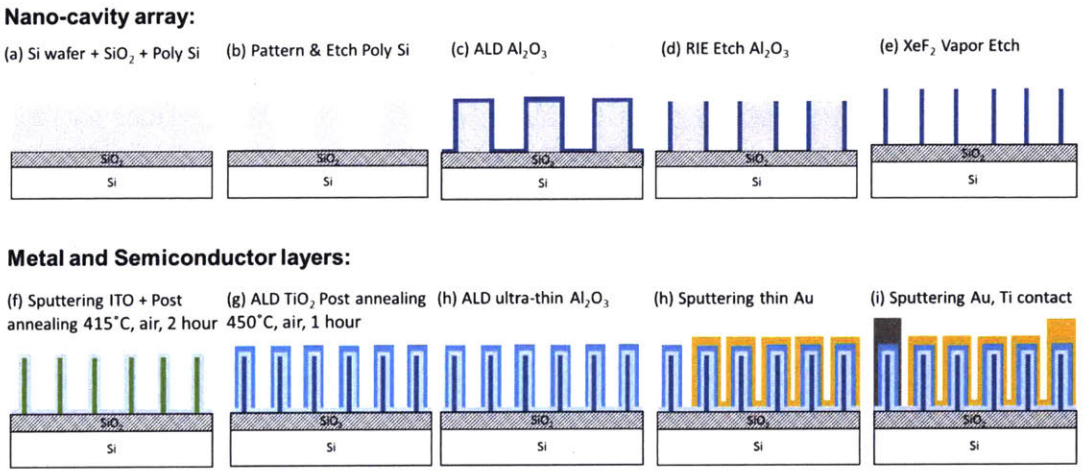

Figure 1.5 Fabrication procedure of MSPhC.

Figure 1.6 shows the photos of fabricated MSPhC by scanning electron microscope (SEM) and focused ion beam (FIB) milling. In Fig. 1.6 (c), the compositions of different layers are shown on the cross-section view of a single nano-cavity. The Pt layer on top and bottom of the nano-cavity was deposited as protective layer for the purpose of imaging. The particle-like structures on the insider wall of the cavity were formed during Pt deposition.

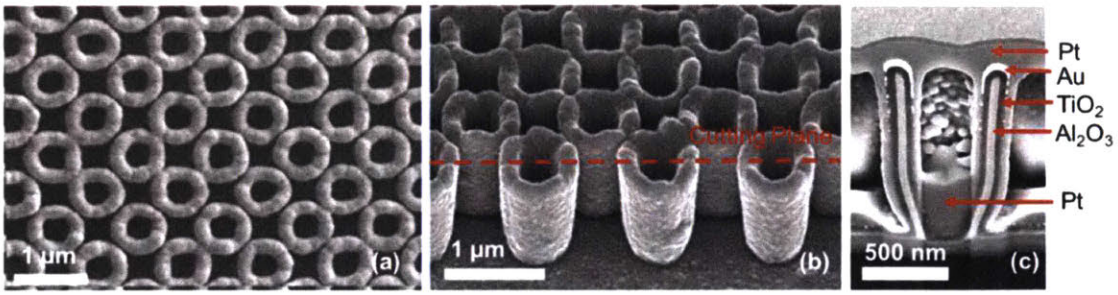

Figure 1.6 Images of MSPhC. (a) Top view with SEM. (b) Titled view at 30° with FIB. The red dash line denotes the position of cross-section view in (c). (c) Cross-section view of a single nano-cavity with FIB.

In summary, we designed the Au/TiO_2 MSPhC with two dimensional nano-cavity array to harvest sub-bandgap solar energy. Through FDTD simulation, the optimized structure dimension was determined to support multiple optical resonance modes inside the nano-cavity and increases the total absorption by MSPhC. The device was fabricated on 6 inch silicon wafer with basic stepper lithography and thin film deposition methods to achieve a large-scale production.

1.3 Surface plasmon for enhanced optoelectronics

Surface plasmon is collective oscillation of conduction electrons in conductor with the electromagnetic field confined at the interface between the conductor and the surrounding dielectric [21]. From the point view of solid state physics, plasmon is the quanta of oscillating electron density wave inside the conductor [22, 23]. It can be classified as propagating waves at the interface, i.e. surface plasmon polariton (SPP) or localized strong electric field oscillation, i.e. localized surface plasmon resonance (LSPR). Surface plasmon can couple light from free space to nano-scale system and serve as a powerful method to manipulate light at sub-wavelength scale. It can also

enhance the intensity of electric field near the interface by orders of magnitude compared with the incident light [21]. This can largely enhance light-matter interaction and absorption by metallic nanostructures that has been designed to generate surface plasmon resonance [24]. In the last decade, extensive efforts have been made to study the application of surface plasmon for energy harvesting and conversion [5, 6, 25, 26]. We will briefly review the theoretical background of surface plasmon and its application in enhanced optoelectronics in the following of this section.

By solving Maxwell's equation for transverse magnetic (TM) mode electromagnetic field (transverse electric mode cannot stimulate SPP [21]) between flat conductor and dielectric, we could get the expression of SPP and its dispersion relation. The derivation of this could be found in many well-known text books. Here we only give the result adopted from Maier [21] without proof. As shown below, at the interface between a dielectric semi-infinite space ($z > 0$) with positive relative permittivity ε_d, and a metal semi-infinite space ($z < 0$) with relative permittivity $Re(\varepsilon_m) < 0$, the solution to propagating wave with evanescent decay in the direction normal to the interface is:

$$H_y(z) = Be^{ik_x x}e^{-k_2 z} \tag{1.2a}$$

$$E_x(z) = iB\frac{k_2}{\omega\varepsilon_0\varepsilon_d}e^{ik_x x}e^{-k_2 z} \tag{1.2b}$$

$$E_z(z) = -B\frac{k_x}{\omega\varepsilon_0\varepsilon_d}e^{ik_x x}e^{-k_2 z} \tag{1.2c}$$

for $z > 0$ and

$$H_y(z) = Be^{ik_x x}e^{k_1 z} \tag{1.3a}$$

$$E_x(z) = -iB\frac{k_1}{\omega\varepsilon_0\varepsilon_m}e^{ik_x x}e^{k_1 z} \tag{1.3b}$$

$$E_z(z) = -B\frac{k_x}{\omega\varepsilon_0\varepsilon_m}e^{ik_x x}e^{k_1 z} \tag{1.3c}$$

for $z > 0$. k_i is real propagation constant along the direction normal to the interface, which causes the decay at the length scale of $1/|k_i|$. k_x is the propagation constant along the interface. ε_0 is the vacuum permittivity. B is a real constant representing the field amplitude. The dispersion relation of SPP at this interface is:

$$k_x = k_0\sqrt{\frac{\varepsilon_d\varepsilon_m}{\varepsilon_d + \varepsilon_m}} \tag{1.4}$$

Where k_0 is the wavenumber of light in vacuum space. The larger the k_x, the smaller the decay length in both the metal and dielectric layer, which means stronger light confinement. Figure 1.7 (a) gives the schematic of SPP at the interface between the dielectric and metal and Fig. 1.7 (b) shows the dispersion relation of it. When the summation of permittivity of the metal and dielectric reaches its minimum, the propagation vector k_x reaches its maximum and we can achieve the strongest light confinement at the interface. The corresponding frequency is called the surface plasmon frequency ω_{SP}.

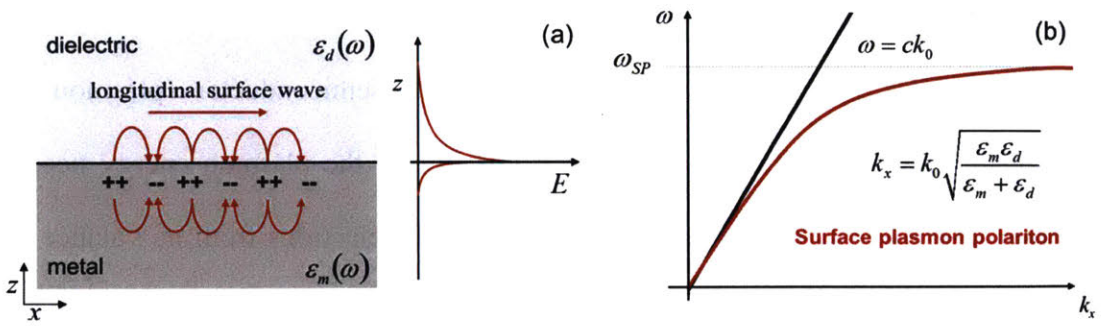

Figure 1.7 Surface plasmon polariton at single flat interface between metal and dielectric. (a) Schematic of SPP at the interface and decay of electric field at direction normal to the interface. (b) Dispersion relation of SPP with surface plasmon frequency ω_{SP}.

On the other hand, for LSPR, the expression of surface plasmon wave and resonant frequency depends on the shape and dimension of metallic nanostructures [21]. Typically, LSPR could be supported on metallic nanoparticles with shapes of sphere [27], rod [28], cube [29] or other random shapes [30]. It is generated as the result of resorting force on conduction electrons caused by the positive charges due to the electric field driven oscillation [22]. For a spherical metallic nanoparticle embedded in dielectric, under the assumption that the dimension of the nanoparticle is much smaller than the wavelength of incident light, the corresponding surface plasmon resonance happens when $\varepsilon_m + 2\varepsilon_d$ reaches its minimum [21].

Plasmonic (metallic-semiconductor) nanostructures could improve solar to electric energy conversion efficiency through the following two major steps [31]. First, photonic enhancement: It improves light absorption inside metal and semiconductor near the interface by generating strongly confined electric field. In this step, an absorbed photon is converted into a plasmon at the interface with the same energy. Second, electron-hole pairs generation and transport: Through non-radiative decay of plasmons, electron-hole

pairs could be generated in metal and transferred into semiconductor (direct electron transfer (DET)) or directly be generated inside semiconductor (plasmon induced resonant energy transfer (PIRET)) [31]. For PIRET the plasmon energy needs to be larger than the bandgap of semiconductor to excite electrons from its valance band to conduction band. On the other hand, for DET, collection of hot electrons generated in metal leads to the harvesting of photon with energy lower than the bandgap of semiconductor. Thus, for the purpose of sub-bandgap solar energy conversion, we will mainly focus on the DET mechanism for hot electron collection. Recent breakthroughs in plasmonic energy conversion have shown that surface plasmon resonance could largely improve the efficiency of hot electron generation and injection [13-15, 32]. Plasmonic devices fabricated with e-beam lithography [15], nanoparticles assembly [32] and nano-imprint lithography [33] show exciting application potentials for solar energy harvesting and photo detection. However, the mechanisms of how surface plasmon enhances the hot electron collection is still under debating, and various theories have been developed [10, 18, 26, 34-36]. In the next section, we will briefly review the theoretical modeling of surface plasmon assisted hot electron collection.

1.4 Theoretical modeling of surface plasmon assisted hot electron collection

The complexity of combining multiscale questions of nano-optical and hot carrier generation makes the understanding of the plasmon assisted hot electron collection extremely difficult [10]. The coupling of light from free space to metallic nanostructure could be solved with classical electromagnetic methods [37], which can provide the

electric field distribution inside the metallic nanostructure. Since the light absorption of metal depends on the net electric filed inside it, which is the superposition of surface plasmon and other optical modes, we will not treat them separately. But surface plasmon will dominate the electric field distribution near the resonance frequency by strongly enhancing the electric field near the interface. After optical coupling, the three steps of hot electron generation, transport and injection could be modeled by quantum mechanical treatments with the information obtained from classical electromagnetic theory [10]. In this section, we will give a brief review of modeling the hot electron collection in Schottky hot carrier devices with metallic nanostructures.

Hot electron generation happens in the time scale of about 10 fs [5, 10]. In metal, non-thermal-equilibrium electrons could be excited through three major mechanisms [24], which are: direct transition (i.e. interband transition), photon-assisted transition and geometry-assisted transition. The last two intraband transition mechanisms rely on the momentum compensation provided by phonon or the surface geometry of metallic nanostructures, and are less likely to happen in bulk metal structure. Material's electronic structure and the effects of nano-scale structures and geometries should be taken into consideration for fully understanding the plasmon assisted hot electron collection process [10]. With band structures of noble metals (like Au and Ag) obtained from density-functional theory [18, 38, 39] the transition of electrons could be studied with Fermi's golden rule [40], which accounts the transition rate of electrons between two different states under the perturbation of electric field. People have found that interband transition will generate hot electrons close to the Fermi surface due to their low D-band

[18, 39]. On the other hand, intraband transition can generate more energetic hot electrons above the Fermi surface. Besides, with the decrease of size of metallic nanostructures, the geometry-assisted transition dominates intraband transition below the interband transition threshold [18]. Geometry-assisted transition could also be analyzed with a simplified method by solving the free-electron like wave equations inside metallic nanostructures, and using Fermi's golden rule to calculate the transition with the Jellium band structure [36, 41, 42]. With these methods mentioned above, we could obtain the initial states of hot electrons with their energy and momentum distribution.

After hot electrons are generated, they could be transferred to the interface between metal and semiconductor. During the transport, hot electrons will lose their energy and momentum through electron-electron and electron-phonon scattering [6, 10, 43]. This thermalization happens in about 10 fs to 100 fs after the excitation [6, 10], and could be evaluated with the electron scattering mean free path at different energy levels [43]. The improvement of plasmon assisted energy conversion efficiency requires a fast transfer of generated hot electrons cross Schottky barriers into semiconductor bands, while the non-equilibrium characteristic makes analyzing this intermediate range charge transport process challenging. Typically, the transport process could be studied either through ultrafast pump-probe measurements (time dependence) [44, 45], or steady state transport at continuous wave illumination (spatial dependence) [10, 46, 47]. Even though a simplified exponential decay model [47, 48] or incorporating a lifetime factor to hot carriers [41] can effectively estimate the transport efficiency, a full analysis of this non-

equilibrium problem should be done by using spatial dependent Boltzmann transport equation [10, 49].

The final step of hot electron collection is the injection across the Schottky barrier. In solid state devices, this has been modeled with the Fowler's theory [11]. Only carriers with enough normal kinetic energy higher than the Schottky barrier, i.e. in an "Escape Cone" in momentum space, could be injected. Fowler's theory and other models [4, 34, 35, 50] based on it always assume that electrons distribute isotropically and uniformly in momentum space. However, recent theoretical calculations [36, 38, 39, 42] and experimental results [14, 15, 51-53] show that in metallic nanostructures, the momentum distribution of generated hot electrons could be largely modified, and the measured IQE does not follow Fowler's theory, especially when surface plasmon resonance exists. Meanwhile the validation of the "Escape Cone" model for roughened surfaces which can provide extra momentum for embedded metallic structures is also debatable [48]. Besides, recent work has demonstrated a plasmon-induced interfacial charge transfer other than the "Escape Cone" model, by directly generating a hot electron on the conduction band of semiconductor and a hot hole in metal, which requires strong inter-coupling and mixing of the electronic levels at the interface and can largely enhance the injection efficiency [14, 54].

In summary, combining the questions of optical coupling in metallic nanostructures with hot electron generation, transport and injection, we could have a complete understanding of hot electron collection in Schottky hot carrier devices. Previously, complex first principle calculations [18, 36, 38, 39, 41, 42] have been applied to study

this process accounting precise band structures of metallic nanostructures with either very small scale (~10 nm) or simple geometries (spherical particles, cubes and rods). Even though these calculations provided us invaluable information about the hot electron collection process, their applicability for complex structures with a relative large scale is limited. For these systems, recent modeling mainly focused on the optical enhancement by surface plasmon resonance [33, 46, 51], with lack of quantum-level mechanisms. A simple but effective model combining classic electromagnetic theories of surface plasmon resonance with microscopic picture of hot electron collection is needed for further understanding and improving the photoresponse of Schottky hot carrier devices.

1.5 Organization of thesis

The goal of this thesis is to analyze the photoresponse of MSPhC device and study the effects of surface plasmon resonance on hot electron collection. We developed an effective model of IQE for Schottky hot carrier devices incorporating the effects of surface plasmon on the momentum distribution of generated hot electrons. It can provide people a guidance for further tuning the IQE and photoresponse by designing the optical coupling of metallic nanostructure with surface plasmon resonance. The organization of this thesis is as following: Chapter 2 provides the detailed characterizations of optical, electrical and photoelectrical properties of MSPhC, from which we evaluated the IQE of this device. A comparison between the experimental observations with previous Fowler's theory is presented, which shows its limited applicability. Chapter 3 analyzes the surface plasmon resonance in MSPhC, and confirms the existence of it under real experimental condition used in photoresponse test. In Chapter 4, we developed the model

to explain the internal photoemission in MSPhC and to estimate the IQE of it. In this model, the energy, momentum and spatial distributions of generated hot electrons are analyzed to estimate the transport and injection efficiencies. We found out that surface plasmon resonance dominates the electric field distribution in the thin Au layer near the resonant wavelength, which generates hot electrons with high enough momentum preferentially normal to the Schottky interface. Our modified model matches the experimental observations better than the previous Fowler's theory. It indicates that the anisotropic momentum distribution should not be ignored when designing Schottky hot carrier devices and we could further tune the IQE and photoresponse by designing the geometry-determined plasmon resonance in the devices. Chapter 5 provides the summary of this thesis work and outlook on further refinement and application of this model.

Chapter 2. Device characterizations of MSPhC

2.1 Absorption by the thin Au layer in MSPhC

In order to extend and enhance the sub-bandgap photoresponse of MSPhC, we have to improve the absorption by the thin Au layer at this range. Through FDTD simulation, we have found the optimized structure dimension of MSPhC to achieve a broadband light absorption from 400 nm to 800 nm. To prove that the thin Au layer contributes to most part of light absorption in the visible range, which is beneficial for hot carrier generation, we calculated the spatial power absorption by different materials with the divergence of Poynting vector [55]:

$$A_i = \frac{1}{2}\omega|E|^2 \operatorname{Im}(\varepsilon_i) \tag{2.1}$$

A_i is the absorption by material *i*, ω is the frequency of light, E is the spatial electric field distribution, and $\operatorname{Im}(\varepsilon_i)$ is the imaginary part of permittivity of material *i*. Through FDTD simulation, electric field profile at different locations were collected to calculate the absorption contribution by different layers.

Figure 2.1 shows the calculated absorption by the thin gold layer (orange line), compared with the total net absorption (brown line) by all of the materials. At the range from 400 nm to 800 nm, the thin gold layer contributes to over 85% of the total light absorption. Due to the light trapping ability of the nano-cavity structure, light-matter interaction time in the Au layer is largely enhanced. Besides, at this range below the bandgap of TiO_2, light will not be absorbed by TiO_2. The rest of the absorption is mainly contributed by the Si substrate. This result indicates that the design can largely improve

the absorption by the metal material, which is crucial for enhancing sub-bandgap photoresponse by hot electron generation in the metal.

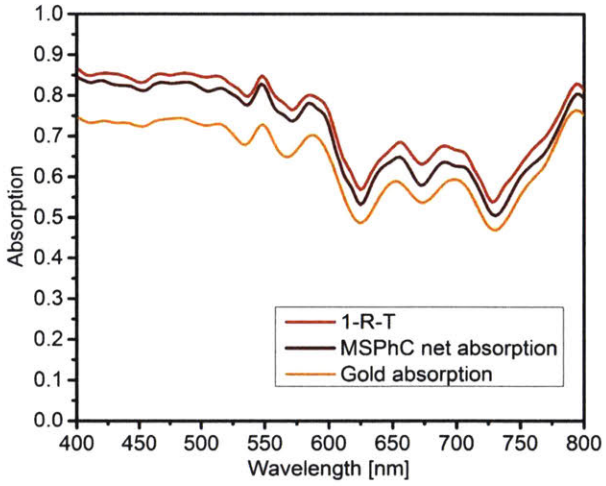

Figure 2.1 Analysis of absorption contribution by the thin Au layer in MSPhC.

In order to prove the validity of the simulation result, we added two frequency-domain monitors on top and bottom of the MSPhC device to record the power flow in and out of it. The net power absorption calculated by $A_{MSPhC} = 1 - R_{MSPhC} - T_{MSPhC}$ is shown as the red line in Fig. 2.1, where R_{MSPhC} and T_{MSPhC} are the reflectance and transmission recorded by the monitors. We can see that the net absorptions calculated by these two methods decently match with each other. The deviation between them is usually caused by the interpolation error of electric field components in FDTD simulation [56]. In most situations, this error is negligible. However, when the electric field component normal to the structure surface is large and when a significant fraction of the total absorption occurs near the surface of the structure, which is what happens in surface plasmon resonance, the error will be significant [57]. Thus, when the simulation involves metallic structures and dielectric interfaces, the mesh size near the interfaces

should be set as small as possible [57]. However, due to the large structure dimension of the nano-cavity, and the three dimensional Au/TiO_2 interface, we can only reduce the mesh size down to 3 nm in X, Y and Z direction to achieve a balance between decent accuracy and efficiency with our computational resources.

Because the MSPhC devices were fabricated on 6 inch silicon wafers, and light cannot penetrate through the wafers, it is difficult to directly measure the absorption by the thin Au layer on it. We can only measure the reflectance of a device with UV-Vis spectrometer (Cary 500, CMSE, MIT). In order to evaluate the absorption by the thin Au layer on a real device, we had to assume that the ratio between it and $1 - R_{MSPhC}$ keeps the same in both FDTD simulations and experiments. With this assumption, the absorption by the thin Au layer on the real device was estimated as:

$$A_{\text{Au-Exp}} = \frac{A_{\text{Au-FDTD}}}{\left(1 - R_{\text{MSPhC-FDTD}}\right)}\left(1 - R_{\text{MSPhC-Exp}}\right) \tag{2.2}$$

$A_{\text{Au-Exp}}$ is absorption by the thin Au layer in a real device, $A_{\text{Au-FDTD}}$ is absorption of the thin Au layer evaluated from FDTD simulation (the orange line in Fig. 2.1), $R_{\text{MSPhC-FDTD}}$ is reflectance of MSPhC evaluated from FDTD simulation and $R_{\text{MSPhC-Exp}}$ is reflectance of MSPhC measured with the spectrometer. Figure 2.2 shows the reflectance of MSPhC and absorption by the thin gold layer obtained from simulations and experiments. We can see that, both simulated and measured results confirm that MSPhC can achieve an evenly low reflectance, i.e. high absorption, from 400 nm to 800 nm, even though the variations in thickness of the thin gold layer and dimension of cavities across the devices fabricated on 6 inch silicon wafers may cause

frequency shift and broadening effects [9]. Based on the assumption mentioned above, the absorption by the thin Au layer on a real device is shown as the solid orange curve in Fig. 2.2. Compared with the simulation result (dash orange curve), the trends and patterns of them match each other quite well.

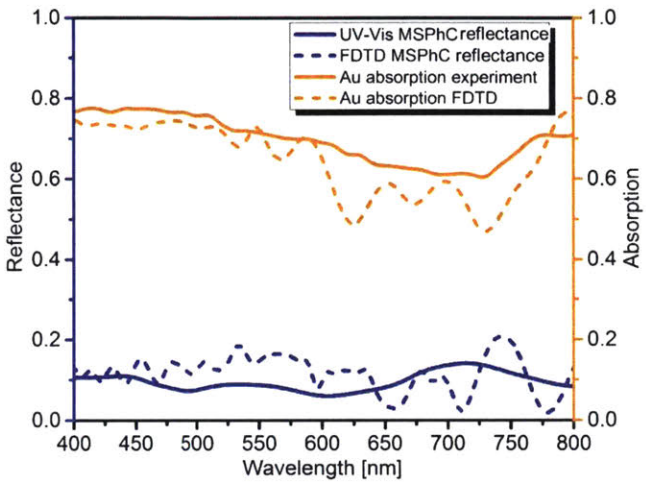

Figure 2.2 Reflectance of MSPhC and absorption of the thin Au layer. Solid blue line: Reflectance of MSPhC from UV-Vis spectrometer measurement. Dash blue line: Reflectance of MSPhC from FDTD simulation. Solid orange line: Absorption by the thin Au layer based on Eq. (2.2). Dash orange line: Absorption by the thin Au layer from FDTD simulation.

In summary, through FDTD simulation and experimental measurement, we characterized the optical properties of MSPhC device. It can achieve a broadband light absorption at the range from 400 nm to 800 nm and the thin Au layer contributes to most part of it. The absorption by the thin Au layer on a real device was estimated and will be used in Section 2.3 to evaluate the IQE of this device.

2.2 Characterization of Schottky barrier height of MSPhC

In a Schottky optoelectronic device, the barrier height determines the threshold of photoresponse [4]. Hot electrons with energy level lower than the barrier height could not be injected onto the conduction band of TiO_2 through internal photoemission. Thus, measuring the barrier height is important for analyzing the hot electron collection process.

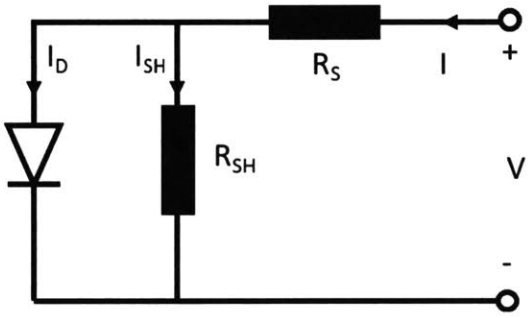

Figure 2.3 Equivalent circuit of a Schottky diode, with shunt resistance of R_{SH} and series resistance of R_S [58].

I-V curve measurement was performed with Keithley 2401 and two point probes to evaluate the barrier height of MSPhC. Figure 2.3 shows the equivalent circuit of a Schottky diode inside an optoelectronic device, which consists of a diode, a shunt resistance and a series resistance [58]. The total current I flow into the diode will be shunted into current I_D which passes through the diode and I_{SH} which passes through the shunt resistance. Based on this circuit model and assuming that the current I_D passing through the Schottky diode is due to thermionic emission, the relationship between current I and voltage V applied at the two ends of the device is [12]:

$$I = I_0\left[\exp\left(\frac{V - IR_s}{nk_BT/q}\right) - 1\right] + \frac{V - IR_S}{R_{SH}} \tag{2.3}$$

and the reverse saturation current I_0 is:

$$I_0 \approx a \cdot A^{**} T^2 \exp\left(-q\phi_B / k_B T\right) \tag{2.4}$$

where n is the ideal factor, k_B is the Boltzmann constant, T is temperature, a is the area of the Schottky diode interface and A^{**} is the Richardson constant (671 A $cm^{-2}K^{-2}$ for TiO_2 [59]). The area a of the Schottky diode in MSPhC was estimated as following. On the 1 cm by 1 cm chip of MSPhC, due to the nano-cavity structure (inner radius of about 250 nm and outer radius of about 450 nm, height of 1000 nm), the effective diode area is about 6.5 times of the chip area. The I-V curve measurement is shown in Fig. 2.4. By fitting it to Eq. (2.3) and Eq. (2.4), the rest of the parameters were estimated to be: $R_S =$ 39 KΩ, $R_{SH} = 8$ MΩ and $n = 1.04$. With these parameters the Schottky barrier height is $q\phi_B = 1.53 \pm 0.11$ eV.

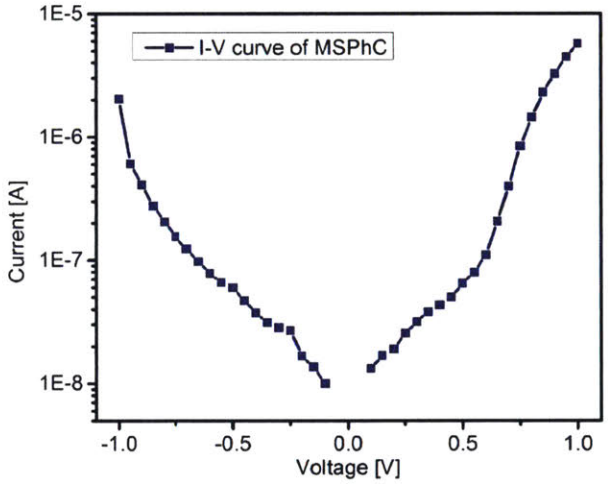

Figure 2.4 I-V curve measurement of MSPhC.

The value we measured on MSPhC is higher than the typical Schottky barrier height between Au and TiO_2 (about 1.0~1.2 eV [6, 16]), which might be caused by the interfacial passive Al_2O_3 layer for improving diode condition [20]. In the following analysis, we will use 1.53 eV as the barrier height of MSPhC.

2.3 Photoresponse and IQE of MSPhC

The photoresponse of MSPhC was measured with a 300 W Xenon arc lamp source monochromated by a holographic diffraction grating. The photocurrent was recorded with Keithley 2401 as the difference between the current when light was on and off. Figure 2.5 shows the equivalent circuit of the MSPhC as an optoelectronic device [58]. Except for the Schottky diode, a source of photo generated current is added. The photocurrent we actually measured is part of the photo generated current after being shunt by the Schottky diode and the shunt resistance.

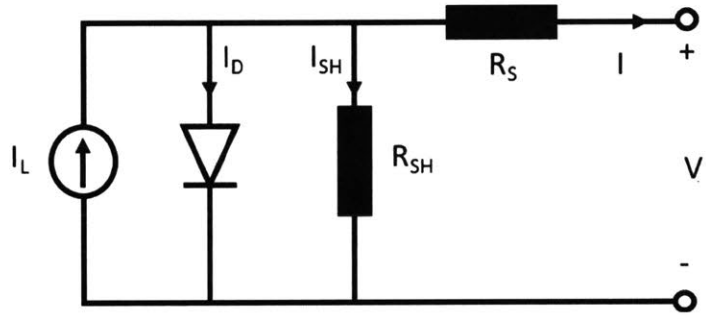

Figure 2.5 Equivalent circuit of MSPhC as an optoelectronic device [58].

Under zero bias voltage, the relationship between photocurrent I as we measured and the photo generated current I_L is [58]:

$$I = I_L - I_0\left[\exp\left(\frac{IR_S}{nk_BT/q}\right)-1\right]-\frac{IR_S}{R_{SH}} \tag{2.5}$$

Compared with the measured I, the second and third terms in Eq. (2.5) are very small and can be neglected. Thus, we can use the measured photocurrent as the photoresponse of MSPhC.

$$I_L \approx I \tag{2.6}$$

Figure 2.6 shows the normalized photoresponse of MSPhC with incident photon energy at the range from 1.55 eV to 3.1 eV (400 nm to 800 nm), which has a sub-bandgap photoresponse with only a single peak at 2.1 eV (590 nm) and a full-width at half-maximum (FWHM) of 235 nm. In contrast to the evenly low reflectance at this range, i.e. high absorption, the photoresponse is largely dependent on the energy of incident photon. In order to understand this, we have to analyze the internal photoemission process in MSPhC.

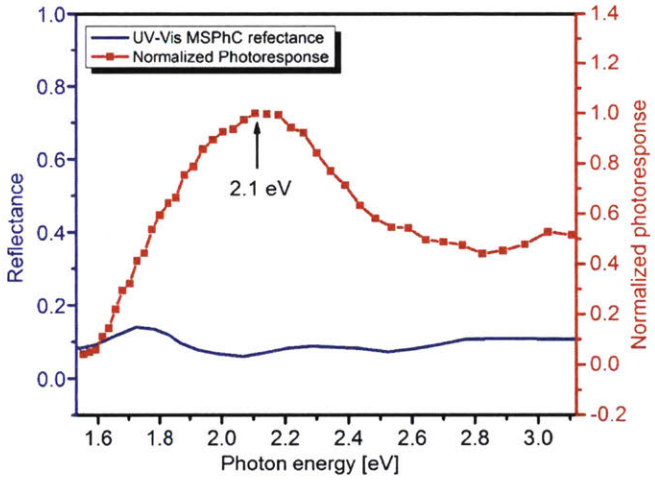

Figure 2.6 Reflectance and normalized photoresponse of MSPhC with photon energy at the range from 1.55 eV to 3.1 eV. Photoresponse measurement shows a sub-bandgap with a peak at 2.1 eV.

Since we added an ultra-thin insulator layer of Al_2O_3 between Au and TiO_2 to improve the diode condition, there will be different hot electron injection mechanisms in MSPhC [20, 60]. Figure 2.7 shows the typical injection mechanisms in a metal/insulator/semiconductor (MIS) junction, where Schottky emission over the barrier, Fowler-Nordheim (FN) tunneling at the edge of the barrier and direct tunneling through the insulator layer could happen [12]. Schottky emission can be modeled with the

assumption of thermionic emission. FN tunneling is the electron tunneling under an intense electric field, which is usually modeled by a triangular barrier edge. Finally, direct tunneling could be modeled as the electron wave being reflected at the metal/insulator and insulator/semiconductor interfaces and decaying inside the insulator layer, which will only happen when the electron's energy is lower than the barrier height.

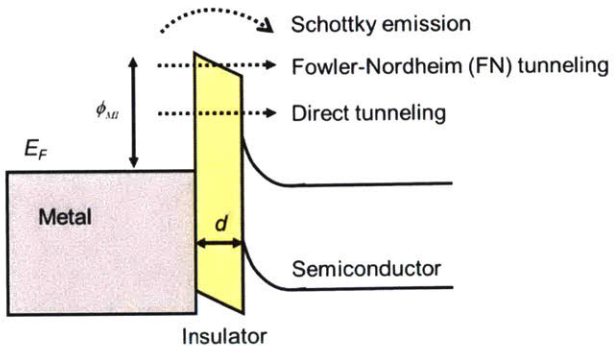

Figure 2.7 Typical electron injection mechanisms in MIS junction.

Photoresponse generated through these three injection mechanisms have different dependence on applied reverse bias voltage and thickness of the insulator layer, as summarized in Table 2.1 [12, 60]. In order to identify the dominating mechanism, we measured the photoresponse vs. reverse bias voltage, since the dependence of photoresponse on insulator thickness for both FN tunneling and direct tunneling are the same.

Table 2.1 Dependence of photoresponse on reverse bias voltage and thickness of insulator layer for different electron injection mechanisms in MIS junction.

Injection mechanisms	Dependence on reverse bias voltage (V)	Dependence on insulator thickness (d)
Schottky emission	$\exp(\sqrt{V})$	$\exp(-\sqrt{d})$
FN tunneling	$V^2 \cdot \exp(-1/V)$	$\exp(-d)$
Direct tunneling		$\exp(-d)$

Figure 2.8 (a) and (b) show the dependence of photoresponse on reverse bias voltage in MSPhC, measured with two lasers at wavelength of 405 nm and 609 nm and reverse bias voltage from 0 V to 0.05 V. For testing Schottky emission mechanism, plot (a) is in scale of $\ln(I)$ vs. $\sqrt{V}$. While for testing FN tunneling mechanism, plot (b) is in scale of $\ln(I/V^2)$ vs. $1/V$. As shown, the Schottky emission mechanism has a better linear fitting result to the measured photoresponse under reverse bias voltage. Thus, we confirmed that Schottky emission dominates the hot electron injection process in MSPhC with incident photon energy at the range from 1.55 eV to 3.1 eV.

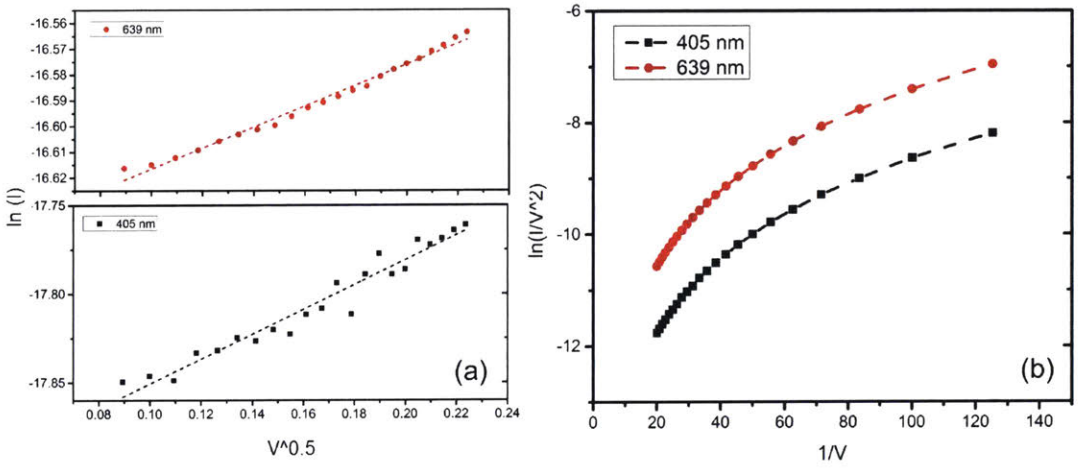

Figure 2.8 Dependence of photoresponse on reverse bias voltage in MSPhC. (a) ln (I) vs. $\sqrt{V}$, for testing Schottky emission mechanism. (b) ln (I/V^2) vs. $1/V$, for testing FN tunneling mechanism.

The IQE of MSPhC was calculated with Eq. (1.1), where the absorption of the thin Au film obtained in Section 2.1 was used. Figure 2.9 shows the normalized IQE of MSPhC. Due to the evenly high absorption, the IQE has the same strong dependence on incident photon energy as photoresponse, with a peak near 2.2 eV. The normalized IQE at 1.55 eV is two orders smaller than the IQE at 2.2 eV, indicating that the threshold of

photoresponse is near 1.55 eV, which matches well with the Schottky barrier height obtained from I-V curve measurement.

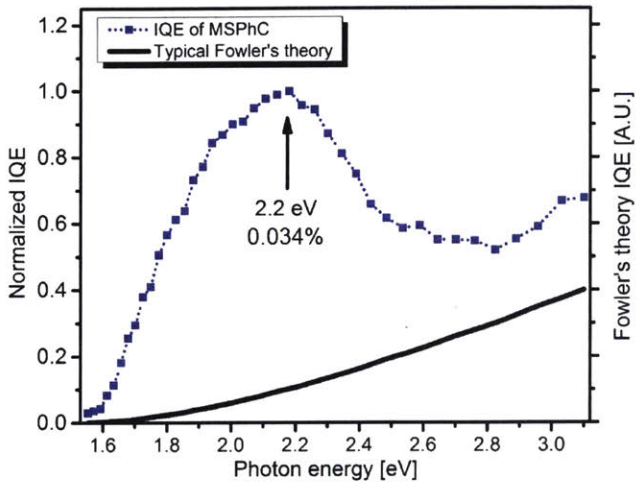

Figure 2.9 Normalized internal quantum efficiency of MSPhC.

We also plotted a typical curve of IQE based on Fowler's theory with barrier height of 1.53 eV and an arbitrary fitting constant C, which is shown as the black curve in Fig. 2.9. It is obvious that Fowler's theory cannot explain the internal photoemission in MSPhC, especially the peak of IQE centered at 2.2 eV.

In summary, measured photoresponse and IQE of MSPhC show a broadband sub-bandgap hot electron collection with incident photon energy from 1.55 eV to 3.1 eV. We confirmed that the dominating hot electron injection mechanism in MSPhC at this range is Schottky emission. However, the widely used Fowler's theory for Schottky internal photoemission could not be applied to explain the dependence of IQE on the incident photon energy. In the following sections, we will analyze the surface plasmon resonance in MSPhC and study its effects on hot electron collection.

Chapter 3. Surface plasmon resonance in MSPhC

3.1 Existence of surface plasmon resonance in MSPhC

Previously, by randomly distributing dipole sources inside the nano-cavity structure, we observed surface plasmon resonance at the interface between Au and TiO_2 along the side wall of the nano-cavity [9]. The resonant wavelength is near 590 nm (2.1 eV) which matches well with the peak of photoresponse and IQE of MSPhC. This suggests that surface plasmon resonance plays an important role in the hot electron collection process. However, in photoresponse measurement, the illumination condition (monochromated Xenon arc lamp source) is closer to a plane wave source instead of dipole sources. It is necessary to test whether MSPhC can generate surface plasmon resonance, and what the resonant wavelength is under this condition.

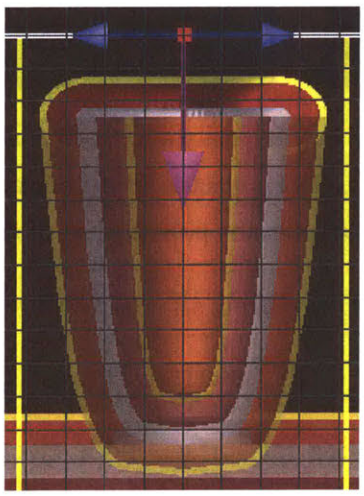

Figure 3.1 FDTD simulation set-up to test the existence of surface plasmon resonance in MSPhC.

We used FDTD simulation to verify the existence of surface plasmon resonance in MSPhC with a plane wave source. The source of a linear polarized light with normal

incident direction was placed on top of the nano-cavity structure, as shown in Fig. 3.1. Profiles of electric field intensity at the cross-section was recorded with a frequency domain monitor. As shown in Fig. 3.2, we observed strong electric field oscillation at the interface between Au and TiO_2 with photon energy at the range from 1.8 eV to 2.1 eV (wavelength of about 590 nm to 700 nm). This electric field oscillation has the same pattern as surface plasmon polariton (SPP) propagating at the interface along the side wall of the nano-cavity.

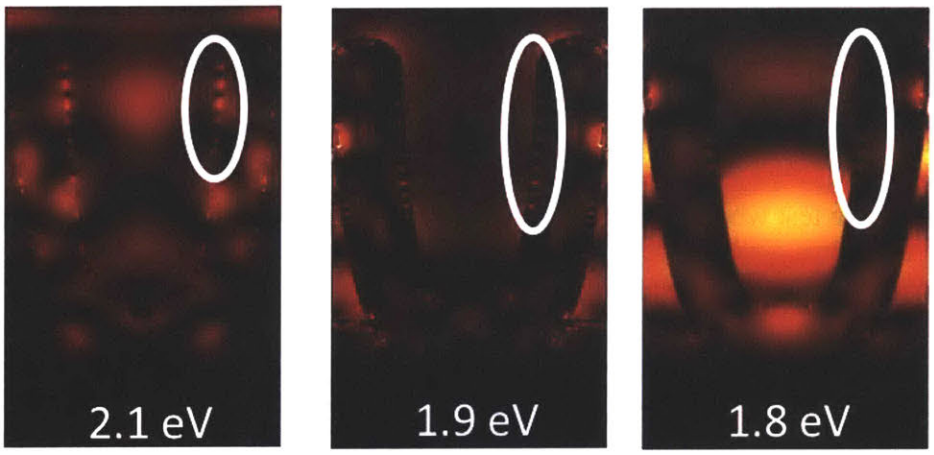

Figure 3.2 Profiles of electric field intensity at cross-section of nano-cavity with photon energy of 1.8 eV, 1.9 eV and 2.0 eV. Strong electric field oscillation is confined at Au/TiO_2 interface with the same pattern as surface plasmon polariton, as shown in the white circles.

In order to confirm that this strong electric field oscillation is SPP, we calculated the dispersion relation of SPP at the interface between planar thin Au and TiO_2 film by solving the Maxwell equation for surface mode electromagnetic wave [21]. Since the inner diameter of the nano-cavity (500 nm) is much larger than the thickness of the thin gold layer (20 nm), this analytical result is a good approximation for SPP propagating along the side wall of the nano-cavity. As shown in Fig. 3.3, considering the effects of the ultrathin layer of Al_2O_3 between Au and TiO_2 and the Au/air interface, the SPP

resonant wavelength will locate at the range from 560 nm to 590 nm (photon energy from 2.1 eV to 2.2 eV), which matches our FDTD simulation. It confirms that under real experimental condition with plane-wave-like source, our structure could support surface plasmon polariton propagating along the Au/TiO_2 interface at the side walls of nano-cavities. However, due to the top and bottom corners of the cavity, SPP is reflected by the two ends and can only propagate along the side walls but cannot propagate between nano-cavities next to each other. Previous literature has named this the confinement of propagating surface plasmon polariton at the side walls of nano-cavity like structure [61, 62]. Assuming that the SPP propagates along the side wall, but is reflected by the up and bottom corners, the wavenumber of SPP is cut off by the height of the nano-cavity, which can only support plasmon standing wave consisting of specific number of half wavelengths. Therefore, we did not observe strong electric field oscillation with photon energy below 1.8 eV (wavelength of 700 nm).

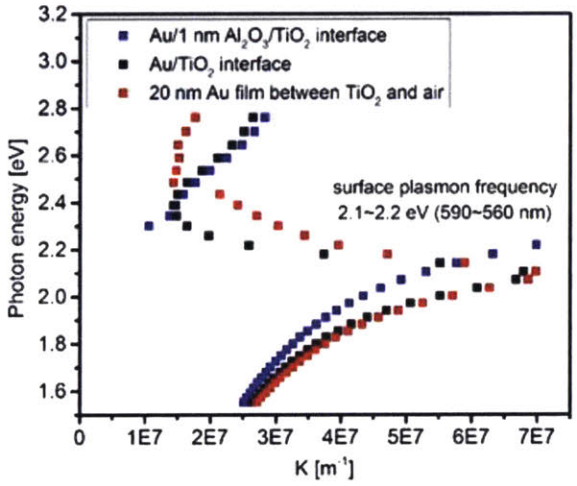

Figure 3.3 Analytical dispersion relation of SPP at planar interface between Au and TiO_2. Black square: planar Au/TiO_2 interface. Blue square: planar $Au/Al_2O_3/TiO_2$ interface. Red square: $air/Au/TiO_2$ interface. The optical constants of materials are adopted from Johnson & Christy [63] and Palik [17].

On the other hand, MSPhC could also support localized surface plasmon resonance (LSPR). For LSPR, the resonant wavelength is largely dependent on the dimension and geometry of metallic nanostructures [21], which can result in various resonant wavelengths other than the SPP resonant wavelength between the same metal and semiconductor. As shown in Fig. 3.2, there are strong electric field oscillations at the top and bottom corners of nano-cavity, which is more likely to be LSPR. In collaboration with Prof. Jouiad's group at Masdar Institute of Science and Technology, we were able to observe similar plasmonic signal around the Au structure on the top corner of the nano-cavity by Electron Energy Loss Spectroscopy (EELS) with an energy filter of 2.08 eV to 2.37 eV, as shown in Fig. 3.4 [64].

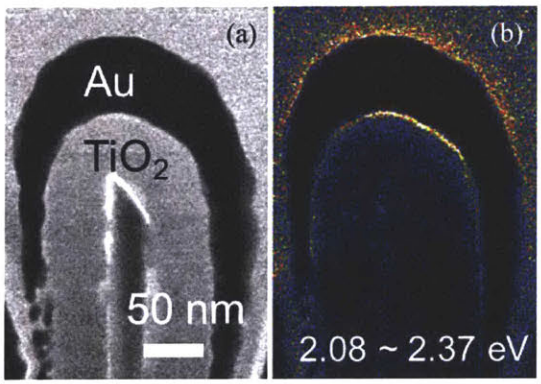

Figure 3.4 EELS image of plasmonic signal around Au structure at the top corner of nano-cavity. (a) Scanning Transmission Electron Microscopy (STEM) cross-section photo of MSPhC. (b) EELS image with energy filter of 2.08 eV to 2.37 eV.

During the sputtering deposition of the thin Au layer on nano-cavities, discontinuous Au nanostructures could form on top of the TiO_2 layer. These isolated Au "islands" could also support LSPR. Figure 3.5 (a) shows the STEM photo of a "fishing hook" (FH) like Au structure near the top of a nano-cavity structure. The nano-cavity was cut into

lamellas with thickness of 70 nm. Figure 3.5 (b) to (e) shows the EELS mapping of this FH structure with incident electron energy from 1.81 eV to 2.22 eV. Plasmonic signals along the transverse and longitudinal direction of the FH structure were observed [64].

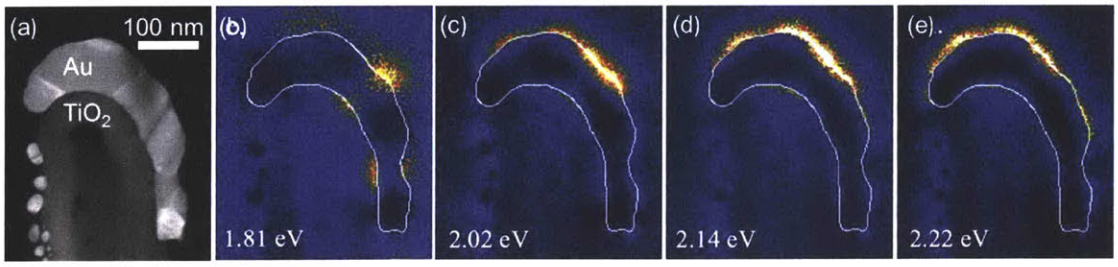

Figure 3.5 EELS mapping of LSPR signals around a "fishing hook" (FH) like structure. (a) STEM photo of the FH structure. (b) to (e) EELS image with incident electron energy from 1.81 eV to 2.22 eV.

We further employed FDTD simulation to confirm the resonant wavelength of LSPR determined by the FH structure. The structure and dimension of the lamella were imported from the STEM photo in Fig. 3.5 (a), with the same thickness of 70 nm. A plane wave source was placed above the lamella with incident direction normal to it. In order to match the LSPR modes, different polarization directions were used for incident light at different wavelengths according to the plasmonic signals shown in Fig. 3.5 (b) to (e). An electric field monitor was placed parallel to the lamella to record the field profile. The profiles representing LSPR are shown in Fig. 3.6, with polarization directions as the white arrows. Strong electric field intensity is represented with red color while weak electric field intensity is represented with blue color. Independent color scales are used in each plot to achieve the best visual expression.

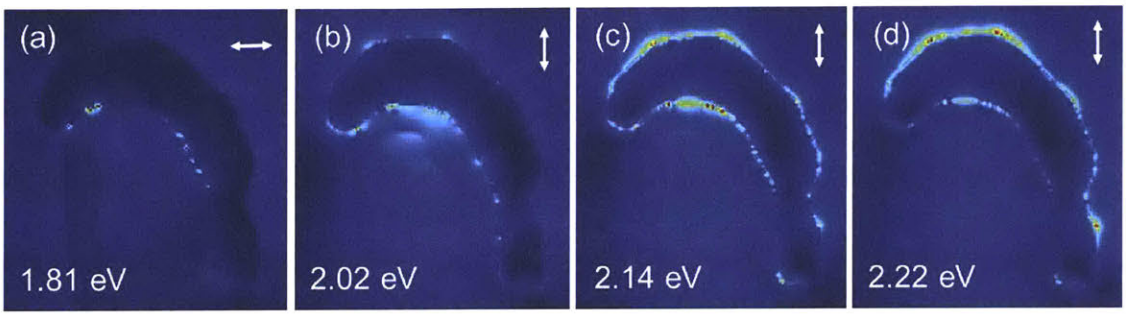

Figure 3.6 FDTD simulation results of electric field profiles around the "fishing hook" (FH) like structure, with incident photon energy from 1.81 eV to 2.22 eV. The polarization directions are shown as the white arrows in each figure.

The plasmonic profile obtained through FDTD simulation matches well with the EELS mapping in Fig. 3.5. At 1.81 eV, transverse LSPR could be supported by the FH structure. While from 2.02 eV to 2.22 eV, longitudinal LSPR were observed.

In summary, through FDTD simulation and EELS investigation, we confirmed that MSPhC could support both SPP at Au/TiO_2 interface along the side wall of nano-cavity and LSPR around discontinuous Au nanostructures formed during fabrication. The resonant wavelengths of both SPP and LSPR match the peak of photoresponse and IQE of MSPhC, which suggests that surface plasmon resonance plays an important role in hot electron collection process. However, when the nano-cavity was cut into lamella for EELS imaging, the illumination condition in both EELS experiments and FDTD simulation may not be the same as the one in photoresponse test. Whether the LSPR modes in photoresponse test are the same as what we observed in FDTD simulations and EELS mapping is unknown. Besides, LSPR is largely dependent on the shape and dimension of metallic nanostructures. For the purpose of simplicity, we may have neglected the possible discontinuity of the thin Au layer in FDTD simulation of MSPhC.

3.2 Effects of surface plasmon resonance on electric field in the thin Au layer

Surface plasmon resonance could generate strong electric field oscillation near the interface between metal and semiconductor [21]. The enhancement of electric field due to surface plasmon decays along the direction normal to the interface. The strongest electric field enhancement could be achieved at the surface plasmon resonant wavelength. Since the absorption by metallic nanostructure is determined by the net electric field distribution inside it, surface plasmon could largely enhance the absorption by the metallic nanostructure within the decay length of surface plasmon to the interface near resonant wavelengths [24].

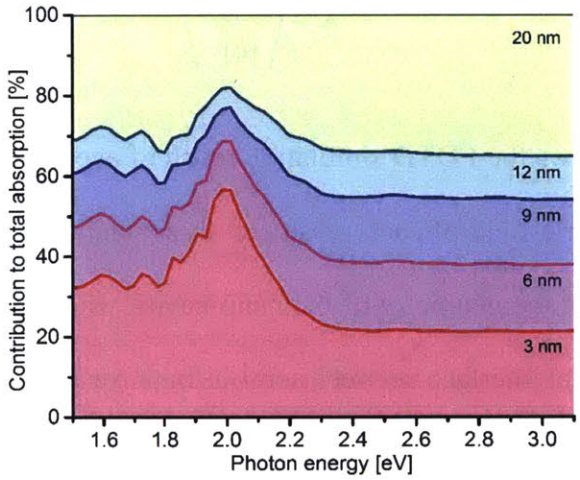

Figure 3.7 Percentage of absorption by the Au layer as a function of thickness to the Au/TiO_2 interface in MSPhC by FDTD simulation.

We studied the enhancement of absorption by the thin Au layer in MSPhC due to surface plasmon resonance through FDTD simulation. Figure 3.7 shows the absorption contribution by the Au layer as a function of normal distance to the Au/TiO_2 interface.

The absorption contribution by Au layer within 3 nm next to the interface increases from 20% to over 50% when photon energy decreases from 2.4 eV to 2.0 eV with a peak near the surface plasmon resonant wavelength, which further confirms the existence of surface plasmon resonance.

Besides, due to the thin thickness of the Au layer in MSPhC, near resonant wavelength, the strong enhancement generated by surface plasmon will dominate the electric field profile inside the thin Au layer. Here we studied the effects of surface plasmon resonance on the electric field inside the Au layer by calculating the averaged ratio between the square of electric field component normal to the Au/TiO_2 interface ($E_\perp$) and square of total electric field (E), which is noted as factor "K".

$$K = \left\langle \frac{|E_\perp|^2}{|E|^2} \right\rangle \tag{3.1}$$

Figure 3.8 shows the FDTD simulation result of averaged K inside the Au layer of MSPhC. The electric field of each mesh cell in simulation was collected. Then K was calculated based on the geometry of the nano-cavity. The red line shows the analytical result of K for SPP at interface between semi-infinite Au and TiO_2, which was calculated with [21]:

$$K_{SPP} = \frac{\left|\sqrt{\varepsilon_{TiO_2}/\varepsilon_{Au}}\right|^2}{\left(\left|\sqrt{\varepsilon_{TiO_2}/\varepsilon_{Au}}\right|^2 + 1\right)} \tag{3.2}$$

The permittivity of Au and TiO_2 were adopted from Johnson & Christy [63] and Palik [17]. Electric field inside the Au layer is dominated by surface plasmon resonance

near the resonant wavelength. As shown in Fig. 3.8, from 1.9 eV to 2.3 eV, the factor K obtained from simulation matches well with the analytical result. Meanwhile the decay of surface plasmon along the direction normal to the interface causes the deviation between simulation and analytical result. Since surface plasmon only dominates electric field within the decay length in metal, the K factor averaged over the thin Au layer in MSPhC will be lower than the analytical result of SPP near the surface plasmon resonant wavelength.

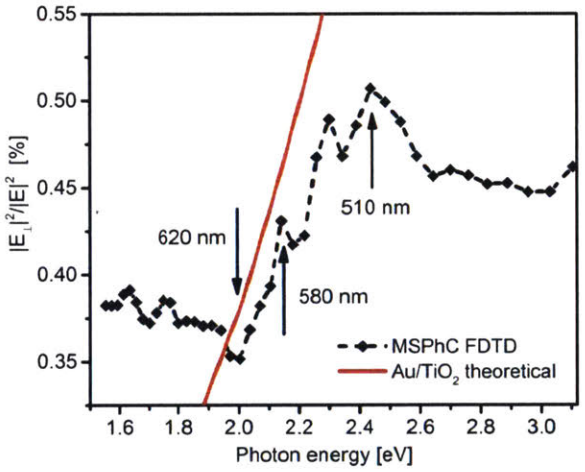

Figure 3.8 Effects of surface plasmon resonance on the factor K in the thin Au layer of MSPhC. Black symbols and dash line: K obtained from FDTD simulation. Red solid line: Analytical result for SPP at interface between semi-infinite Au and TiO_2.

In summary, thorough analyzing FDTD simulation results, we found that surface plasmon resonance could generate strong electric field oscillation confined at the interface between Au and TiO_2 in MSPhC, which largely enhances the absorption by the thin Au layer within decay length to the interface and dominates the electric field profile inside the Au layer.

Chapter 4. Modeling effects of surface plasmon resonance on hot electron collection in MSPhC

In previous chapter, we confirmed the existence of surface plasmon resonance in MSPhC at a wavelength near 590 nm, which matches well with the peak of photoresponse and IQE. We also found out that near the resonant wavelength, surface plasmon dominates the electric field distribution inside the thin Au layer. Since the light absorption by metallic nanostructures is determined by the net electric field distribution in it, surface plasmon will largely affect the hot electron generation near the resonant wavelength. In order to understand the internal photoemission in MSPhC, we combined the question of electric field distribution, which could be solved with classical electromagnetic tools like FDTD simulation, with the question of hot electron generation, which needs to be analyzed with quantum-level theories. As shown in Fig. 4.1, the internal photoemission process could be divided into three steps [10, 34, 35]: (1) hot electron generation, (2) transport to the interface and (3) injection across the junction. After generated with initial energy and momentum at different locations inside the metal, hot electrons travel with scattering against electrons, phonons and defects, and a part of them can reach the metal-semiconductor interface. At the interface, hot electron injection can happen if the normal component of hot electrons' kinetic energy is higher than the Schottky barrier [4, 34]. With the information of electric field distribution obtained from FDTD simulation, we analyzed effects of surface plasmon on hot electrons' energy, momentum and spatial

distribution, and developed a model to predict the IQE of this metallic-semiconductor Schottky device [65].

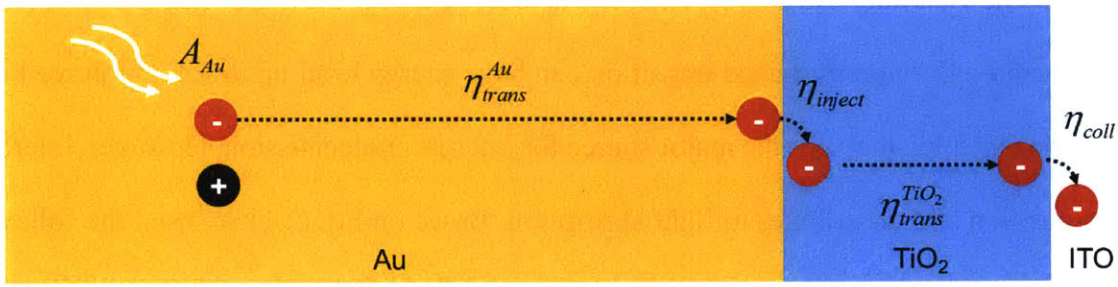

Figure 4.1 Hot electron collection process in MSPhC. Hot electrons generated in the thin Au layer by absorbing a photon will be transferred to the interface between Au and TiO_2 with scattering loss. At interface, hot electrons with enough normal kinetic energy could be injected over the Schottky barrier to the conduction band of TiO_2, and finally be collected at the back contact of ITO. The IQE of MSPhC will be proportional to the transport efficiency in side Au and injection efficiency over the Schottky barrier.

4.1 Hot electron generation

4.1.1 Energy distribution of hot electrons

The election excitation mechanisms in metal could be divided into interband transition (D to S band) and intraband transition (S to S band) [18, 24]. Nanoscale geometries provides required momentum for intraband transition, which makes it preferable for intraband transition to happen in metallic nanostructures. First principle calculations [18, 39] and experimental work [46] have shown that the intraband transition dominates light absorption below the interband transition threshold, and generates highly energetic hot electrons. On the other hand, below the threshold interband transition dominates light absorption and generates low energy hot electrons close to the Fermi level [18, 39]. Since D band of gold locates about 2 eV below the Fermi level [6, 34], hot electrons excited

through interband transition by absorbing a single photon with energy from 1.55 eV to 3.1 eV (wavelength from 400 nm to 800 nm) will probably not have energy level higher than the Schottky barrier of 1.53 eV in our case. On the other hand, hot electrons generated through intraband transition can have energy level up to 3.1 eV above Fermi surface, which makes it the major source for internal photoemission. However, interband transition still contributes to light absorption. Based on Eq. (2.1) we used the following method to decompose the light absorption by the Au layer through interband and intraband transition:

$$A_{\text{intra}} = A_{Au} \frac{\text{Im}(\varepsilon_{\text{intra}})}{\text{Im}(\varepsilon_{\text{intra}} + \varepsilon_{\text{inter}})} \tag{4.1a}$$

$$A_{\text{inter}} = A_{Au} \frac{\text{Im}(\varepsilon_{\text{inter}})}{\text{Im}(\varepsilon_{\text{intra}} + \varepsilon_{\text{inter}})} \tag{4.2a}$$

A_{intra} and A_{inter} are the absorption by intraband and interband transition in Au. $\varepsilon_{\text{intra}}$ and $\varepsilon_{\text{inter}}$ are the intraband contribution and interband contribution to the permittivity of Au. $\varepsilon_{\text{intra}}$ could be estimated with Drude model [66]. The values of them in optical range were adopted from Johnson & Christy [63].

Figure 4.2 plots the absorption contribution by interband and intraband transition and total absorption in the thin Au layer in MSPhC. Below about 620 nm (2.0 eV), interband transition contributes to most part of the total absorption and hot electron generation. Above the threshold, hot electrons generated through intraband transition dominates the absorption of light.

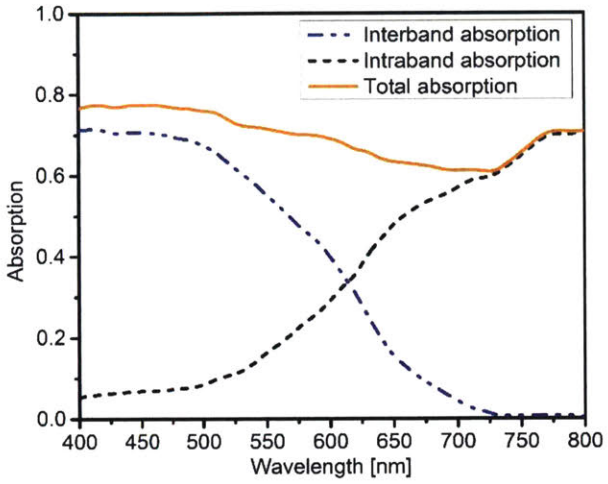

Figure 4.2 Absorption contribution by interband and intraband transition in the Au layer in MSPhC.

Since only intraband transition contributes to hot electron collection in our case, we will mainly focus on analyzing the energy, momentum and spatial distribution of hot electron generated through this mechanism. As mentioned in introduction, electron excitation through intraband transition in Au could be modeled with a free-electron-like Jellium model with Fermi energy level at 5.5 eV [34, 35]. With this simplified band structure, electrons could be excited from an energy level E_0, below the Fermi level E_F in the range $E_F - h\nu \leq E_0 \leq E_F$, to an energy E_1 level in the range $E_F \leq E_1 \leq E_F + h\nu$ by absorbing a photon with energy $h\nu$. The distribution of generated hot electrons' energy depends on the probability of each transition between two different energy levels. Here we use electron distribution joint density of states (EDJDOS) to evaluate the number of possible electron transitions between two specific states [34, 35, 50]:

$$D(E_0 + h\nu, h\nu) = \rho(E_0) f(E_0) \rho(E_0 + h\nu) f(E_0 + h\nu) \tag{4.3}$$

$D(E_0 + h\nu, h\nu)$ is the EDJDOS of exciting a hot electron from energy level E_0 by absorbing a photon with energy $h\nu$. $\rho(E)$ is the density of states (DOS) of the electrons at energy level of E, which is proportional to $E^{1/2}$ given the free-electron-like band structure. $f(E)$ is the Fermi-Dirac distribution function. Then energy distribution of generated hot electrons could be calculated with the probability G of generating a hot electron from the energy level E_0 by absorbing a photon with energy $h\nu$:

$$G(E_0 + h\nu, h\nu)dE = \frac{D(E_0 + h\nu, h\nu)dE}{\int_{E_F - h\nu}^{E_F} D(E + h\nu, h\nu)dE} \tag{4.4}$$

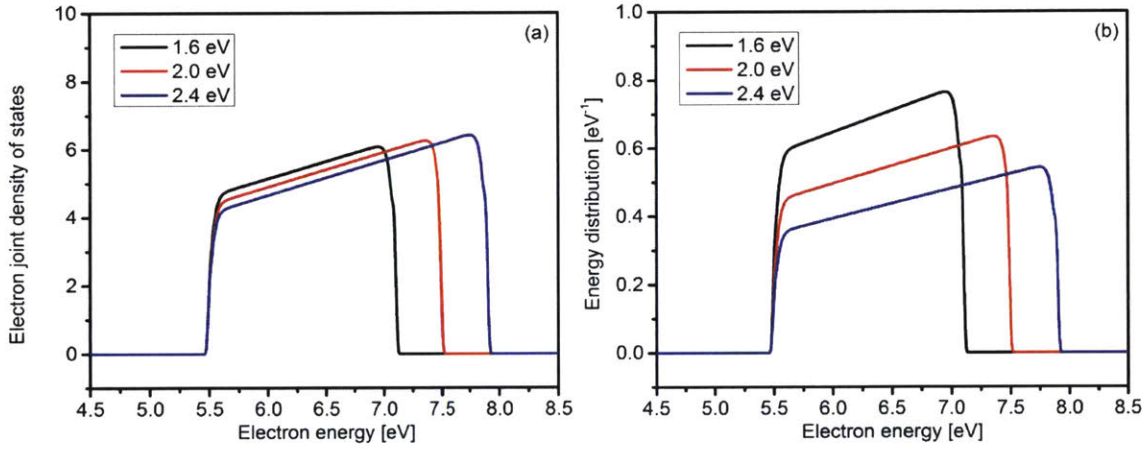

Figure 4.3 Energy distribution of hot electron generated through intraband transition in Au. (a) EJDOS of hot electrons generated by absorbing a photon with energy of 1.6 eV, 2.0 eV and 2.4 eV. (b) Corresponding energy distribution of generated hot electrons.

Figure 4.3 shows the EJDOS and energy distribution of hot electrons generated through intraband transition in Au by absorbing a photon with energy of 1.6 eV, 2.0 eV and 2.4 eV, based on Eq. (4.4) with dE = 0.02 eV and the free-electron-like Jellium model. We can see that the distribution of hot electrons locates from E_F to E_F+$h\nu$, with the pattern determined by the free-electron-like band structure. The area below the

energy distribution curve in Fig. 4.3(b) equals to 1. This kind of simplification has been successfully applied on a wide range of noble metals [67]. While a more realistic energy distribution could be obtained by EJDOS method with the real band structure of metals [50].

4.1.2 Momentum distribution of hot electrons

In previous theories of Schottky internal photoemission, momentum distribution of hot electrons were always assumed to be isotropic and uniform [34, 35, 50], which is a key assumption in Fowler's theory [11]. However, recent theoretical [36, 41, 42] and experiment [51, 52] works have shown that photoresponse is proportional to the electric field normal to the metal-semiconductor interfaces, which suggests that the momentum distribution of generated hot electrons is not isotropic but depends on the electric field inside metallic structure. Following the methods developed by Govorov *et. al.* [36] we could have a deep insight into the effects of electric field on hot electron momentum distribution. In metallic nanostructures, the nanoscale geometry provides required momentum for intraband transition, which dominates the hot electron excitation below the interband transition threshold. By solving the Schrödinger equation for free electrons in metallic nanostructure, and using Fermi's golden rule with optical matrix induced by surface plasmon, we can calculate the hot electron generation rate and momentum distribution in the metallic nanostructure. With this method, people have investigated energy and momentum distribution of hot electrons in metallic nanostructures like nano sphere [41], cube and platelet [36]. They found out that, in momentum space, the transition rate by changing a specific wavenumber of the Jellium electron wave function

is proportional to the square of the electric field along that direction. Thus, surface plasmon can significantly enhance the hot electron generation rate by generating strong electric field oscillation near the metal-semiconductor interface [41, 42]. Further, near resonant wavelength the momentum distribution of generated hot electrons is determined by the electric field profile and the geometry of metallic nanostructure, which defines the wave function of electrons and provides momentum for transition [36].

For example, we applied this method on gold nano rods, similar work could also be found in previous literature [42]. When the polarization of incident light is parallel to the longitudinal axis of the nano rod, and the dimension of the nano rod is much smaller than the wavelength of incident light, in momentum space, only wavenumbers along the longitudinal direction changes. In Fig. 4.4, we plot a schematic of momentum distribution of hot electrons in a nano rod with aspect ratio of 3:1, when the electric field is parallel to the longitudinal axis *Z*. For the purpose of easy observation, the plot is two dimensional. The momentum distribution is largely modified by the electric field. Only the momentum component along the longitudinal axis changes.

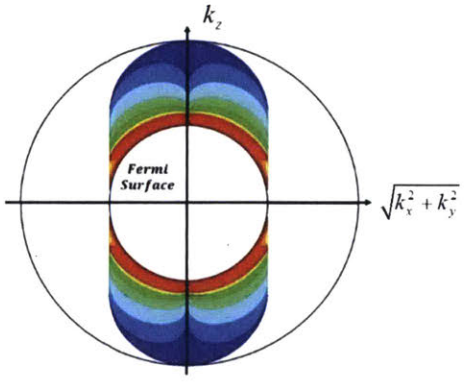

Figure 4.4 Schematic of hot electron momentum distribution generated by longitudinal electric field inside a gold nano rod. High distribution probability is represented with red color while low distribution probability is represented with blue color. Only longitudinal momentum changes.

Based on these previous results and the requirement of energy conservation, a model describing the momentum distribution of hot electrons is developed [65], which has been neglected in previous theories of Schottky internal photoemission. In momentum space, the probability of electron transition between two energy levels by changing a specific wave number is proportional to the square of electric field along that direction. Then, the integration of probability P of generating a hot electron with momentum (k_x, k_y, k_z) on a surface of constant energy needs to satisfy:

$$\iiint_{|k|^2=\text{constant}} P\left(k_x,k_y,k_z\right)\cdot\frac{k_i^2}{k_x^2+k_y^2+k_z^2}dk_x dk_y dk_z=\left\langle\frac{|E_i|^2}{|E|^2}\right\rangle \tag{4.5}$$

Since in our case we care more about the kinetic energy component normal to the interface, we chose the electric field component normal to the interface $E_\perp$ as E_i. Thus the right hand side of Eq. (4.5) is actually the factor K we defined in Section 3.2. This averaged restriction of momentum distribution combines the electric field distribution with hot electron generation. Surface plasmon could largely modify the momentum distribution by control the electric field inside metallic nanostructure near resonant wavelengths.

A first order approximation of momentum distribution that can satisfy the above averaged restriction is:

$$P(\theta)=\frac{1}{2}\sin(\theta)+\frac{12\cdot K-4}{3\pi}\cos(2\theta) \tag{4.6}$$

θ is the angle against the normal direction to the interface. We did not treat the other two in-plane directions differently because they are tangential to the interface and do not affect the momentum distribution regarding the normal direction. Thus the distribution could be simplified as a function of θ. In Eq. (4.6), the second term on the right hand side represents the effect of internal electric field on the momentum distribution. Need to notice that Eq. (4.6) is only a first order model satisfying the restriction of Eq. (4.5). The value of K is limited ($1/3 \leq K \leq (3\pi + 8)/24$) to satisfy that $P(\theta) \geq 0$ for $\theta \in [0, \pi]$. A more realistic momentum distribution in nano scale system could be calculated with the random phase approximation method used in previous theoretical works [36, 41, 42]. However it relies on knowing the exact electron's wave equations and has only been applied to simple small geometries such as nanoparticles or bulk materials. Our model, on the other hand, could be applied to more complex and larger scale systems, like MSPhC. In the following sections, we will show that this simplified first order approximation could effectively represent the anisotropic momentum distribution of hot electrons in MSPhC, and can further achieve a decent prediction of IQE for this device.

Based on Eq. (4.6), Fig. 4.5 shows the anisotropic momentum distribution of hot electrons on a surface of constant energy when incident light is at 510 nm, 580 nm and 620 nm. z is the direction normal to the interface. It clearly shows that the momentum distribution of hot electrons is not isotropic due to the effect of internal electric field. A higher K will cause the concentration of hot electron distributed along the direction normal to the interface. Near resonance frequency, highest factor K of about 0.5 could result in an enhancement factor of over 7 times, compared with isotropic momentum

distribution, which enhances the number of hot electrons locating inside the "Escape Cone" area. This indicates that the anisotropic momentum distribution can affect the hot electron injection and should not be neglect when modeling internal photoemission process.

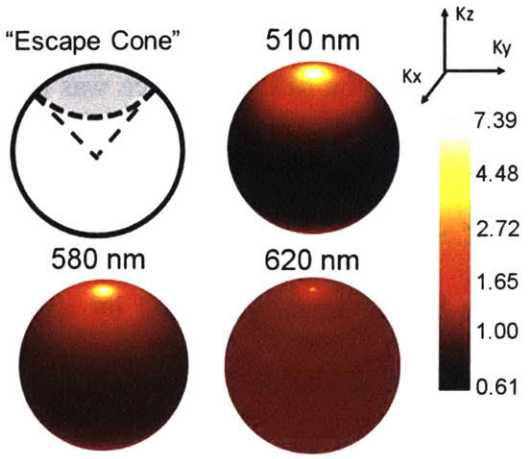

Figure 4.5 Anisotropic hot electron momentum distribution caused by surface plasmon resonance. The scale bar shows the distribution probability normalized against isotropic distribution in natural log scale. Left upper corner shows the schematic of "Escape Cone" model.

4.1.3 Spatial distribution of hot electrons

Since surface plasmon resonance could generate strong electric field near the Au/TiO_2 interface, it will increase the Au layer absorption within the decay length, as we discussed in Section 3.2. We used the FDTD simulation result of absorption by the Au layer as a function of distance to the Au/TiO_2 interface to represent the spatial distribution of hot electrons. Because the generation of hot electrons depends on the net electric field distribution, we did not distinguish the mechanisms due to surface plasmon

decay and others. Instead, the effects of surface plasmon resonance were treated together with other optical modes as a superposition. Compared with hot electrons generated through other "bulk" paths of intraband transition, plasmonic hot electrons are generated closer to the interface, which reduces the possible scattering loss during transport.

4.2 Hot electron transport

In photoresponse measurement, the MSPhC device was under continuous illumination to achieve a steady state hot electron transport. Thus, the transport efficiency could be estimated with a simplified spatial dependent exponential decay model [47, 48]. The averaged probability for hot electrons generated by absorbing a single photon with energy hv to reach the metal-semiconductor interface is:

$$P_{\text{transfer}}(hv) = \int_0^{H_{Au}} \eta(hv, h_{Au}) \exp\left(-h_{Au}/l_{\text{mfp}}\right) dh_{Au} \tag{4.7}$$

where h_{Au} is the normal distance to the interface, H_{Au} is the thickness of Au layer, $\eta(hv, h_{Au})dh_{Au}$ is the percentage of absorption by the thin layer dh_{Au} with distance h_{Au} to the interface. l_{mfp} is the mean free path (MFP) of hot electrons, which equals to [35]:

$$l_{mfp}^{-1} = l_{ee}^{-1} + l_{ep}^{-1} \tag{4.8}$$

l_{ee} is electron-electron scattering MFP and l_{ep} is electron-phonon scattering MFP. Experimental measurement have shown that the electron MFP depends on electron's energy [35]. l_{ee} is in the range of 10~100 nm, while l_{ep} is in the range of 10~100 nm of hot electrons within 6 eV above the Fermi level [35]. For simplicity, here we fix the mean free path as l_{mfp} =10 nm for hot electrons from Fermi level to about 3 eV above

[47]. Figure 4.6 shows the averaged transport probability of hot electrons in MSPhC as a function of photon energy. We can see that near resonant wavelength, the enhancement of absorption near the interface caused by surface plasmon largely improves the hot electron transport efficiency. Therefore, surface plasmon could enhance IQE and photoresponse of Schottky hot carrier devices by reducing the transport distance and scattering loss of generated hot electrons before injection through the metal-semiconductor interface.

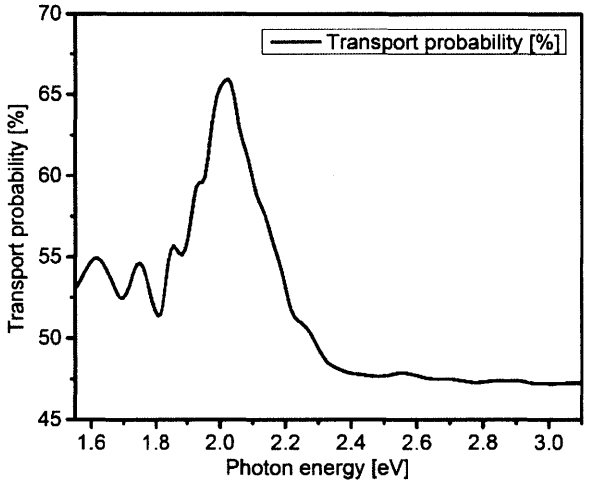

Figure 4.6 Averaged transport probability of hot electrons in MSPhC to reach the Au/TiO_2 interface.

4.3 Hot electron injection

To model the injection probability when hot electrons reach the Schottky interface, we still use the "Escape Cone" model [11] while incorporating the effect of anisotropic momentum distribution caused by surface plasmon resonance. Hot electrons with normal kinetic energy larger than the Schottky barrier height have injection probability of 1 while the others have injection probability of 0 [4, 35, 38, 68]. This criteria allows us to

obtain an analytical expression of the injection probability, while more delicate models based on calculating the transmission coefficient of electrons over a rectangular potential step and considering the effects of electrons effective mass jump across the interface could also be found in literature [68]. The injection probability P_{inject} of a hot electron at energy level $E_h \geq E_F + q\phi_B$ is:

$$\begin{aligned} P_{\text{inject}}(E_{\text{h}}) &= \int_0^{\Omega_{\text{escape}}} P(\theta)\, d\theta \\ &= \frac{1}{2}\left(1 - \sqrt{\frac{q\phi_B + E_F}{E_{\text{h}}}}\right) + \frac{6K-2}{3\pi}\left[\sqrt{\frac{q\phi_B + E_F}{E_{\text{h}}}}\sqrt{1 - \frac{q\phi_B + E_F}{E_{\text{h}}}}\right] \end{aligned} \tag{4.9}$$

The escape angle Ω_{escape} is defined as $\cos(\Omega_{escape}) = \sqrt{(q\phi_B + E_F)/E_h}$. The first term on the right hand of Eq. (4.9) is equivalent to the injection probability in Fowler's theory [4], while the second term reflects the effects of anisotropic momentum distribution, which has not been considered by previous theories. When K is larger than 1/3, the concentration of hot electron along the direction normal to the metal-semiconductor interface will enhance the injection probability.

Figure 4.7 shows the injection probability of hot electrons excited by absorbing a single photon with energy of 1.6 eV, 2.0 eV and 2.4 eV. The corresponding K factors in MSPhC at these three photon energies are 0.38, 0.35 and 0.50 respectively. At the same electron energy level, a larger factor K results in stronger concentration of hot electrons along the direction normal to the Au/TiO_2 interface in momentum space, which can increase the injection probability. Therefore, surface plasmon resonance could also enhance IQE and photoresponse by increasing injection probability of hot electrons through modifying the hot electron momentum distribution.

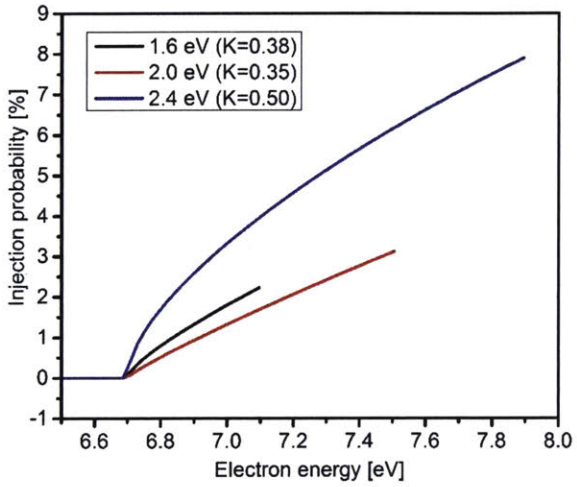

Figure 4.7 Averaged injection probability of hot electrons generated by absorbing a single photon with energy of 1.6 eV, 2.0 eV and 2.4 eV in MSPhC.

4.4 Prediction of IQE for surface plasmon assisted Schottky hot carrier devices

Combing all of the above analysis of hot electron generation, transport and injection together, the IQE of a Schottky device as a function of photon energy can be calculated with [65]:

$$\eta_{\mathrm{IQE}}(h\nu)=\frac{A_{\mathrm{intra}}}{A_{\mathrm{intra}}+A_{\mathrm{inter}}}P_{\mathrm{transfer}}\cdot\int_{E_F+q\phi_B}^{E_F+h\nu}G(E_h,h\nu)P_{\mathrm{inject}}(E_h)dE_h \tag{4.10}$$

Even though interband transition does not contribute to photocurrent, it still contributes to light absorption and IQE. Thus it is necessary to consider its effect at range above the interband transition threshold.

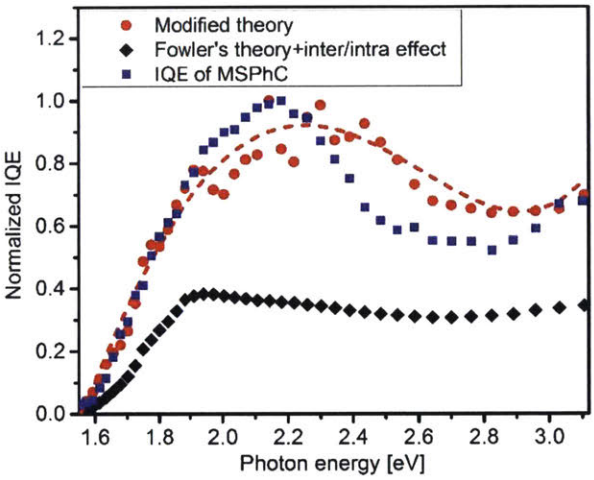

Figure 4.8 Normalized IQE of MSPhC based on the modified model and Fowler's theory. The predictions of these two models are compared with experimental results.

Figure 4.8 shows the normalized IQE calculated with our model and Fowler's theory incorporating the effects of interband transition. The IQE is affected by both the intrinsic properties of Au and external effects of nanostructure and illumination condition. The black symbols of IQE based on the assumptions of Fowler's theory only considers the effects of inter- and intraband transition, i.e. the band structure of Au. Basically it only uses the first term in Eq. (4.9) to calculate the injection probability, which does not consider the effects of anisotropic momentum distribution. It shows the platform shape of IQE due to interband transition. On the other hand, the anisotropic momentum distribution caused by SPP largely enhances the IQE with a peak near 2.2 eV. The pattern predicted by our model matches with the IQE of MSPhC better than the widely used Fowler's theory. This results indicates that the effects of anisotropic electron momentum distribution by surface plasmon should be considered when designing Schottky hot carrier devices [25]. A device that can generate hot electrons with momentum

preferentially normal to the Schottky interface can largely enhance the device's IQE. Need to notice that several factors may cause the deviation between the predicted value and the experimental observation of IQE. For example, we did not consider the transport efficiency inside TiO_2 and the collection efficiency at the back contact. Further, a more realistic momentum distribution of hot electron could also reduce the deviation.

In summary, by incorporating the effects of surface plasmon resonance on modifying momentum distribution to enhance hot electron injection efficiency and on reducing scattering loss during hot electron transport, we developed a model to predict the IQE of surface plasmon assisted Schottky hot carrier devices. Compared with the widely used Fowler's theory, our model can better and effectively represent the internal photoemission in surface plasmon assisted hot electron collection process.

Chapter 5. Conclusion

5.1 Summary

In summary, the effects of surface plasmon resonance on internal photoemission in MSPhC is investigated in this work. Although the two dimensional nano-cavity array of MSPhC could achieve a broadband light absorption by supporting multiple optical modes, only surface plasmon resonance can largely enhance the IQE. Through FDTD simulation and analytical calculation, we confirmed the existence of surface plasmon resonance in MSPhC with a resonant wavelength near 590 nm, which matches well with the peak of sub-bandgap photoresponse. By generating strong electric field oscillation near Au/TiO_2 interface, surface plasmon resonance dominates the electric field distribution inside the thin Au layer. It increases the electric field component normal to the interface, which can significantly modify the momentum distribution of hot electrons generated through geometry assisted intraband transition in metallic nanostructures. Near resonant wavelength, in momentum space hot electrons concentrate along the direction normal to the interface, which can largely enhance the injection efficiency over the Schottky barrier. Moreover, surface plasmon resonance enhances the absorption by the Au layer near the interface and reduces scattering loss of hot electrons. Considering these effects of surface plasmon resonance on hot electrons generation, transport and injection, we developed a model to predict IQE of surface plasmon assisted Schottky hot carrier devices. It achieves a decent match with our experimental observations of MSPhC's photoresponse, which cannot be explained by the widely used Fowler's theory.

5.2 Outlook

This work provides a method that combines large scale photonic design with quantum-level tools, which could serve as a guidance for designing Schottky hot carrier devices. As shown in Fig. 5.1, the information of electric field, for example *K*, in plasmonic metallic nanostructures could be obtained from classical electromagnetic tools like FDTD simulation. These factors could be applied to determine the energy, momentum and spatial distribution of generated hot electrons with the information of the metal's intrinsic properties, which can be obtained with quantum-level tools like DFT and *ab-initio* calculation. Finally, with our model of internal photoemission and states of generated hot electrons, the IQE and photoresponse of the device can be predicted.

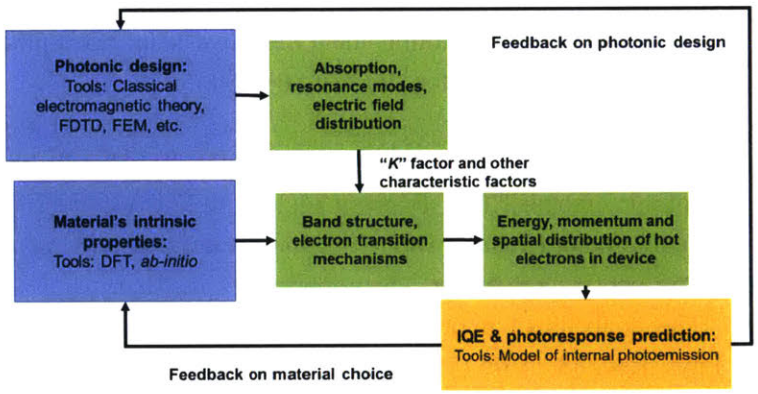

Figure 5.1 Design flow for surface plasmon assisted Schottky hot carrier devices, combining large scale photonic design with quantum-level tools.

Moreover, the applicability of this model to different device architectures needs to be studied. Factors that may influence the applicability include structure dimension and geometry, model of hot electron momentum distribution in various metal materials and injection mechanisms other than Schottky internal photoemission. It would be helpful to further refine this model for more widely application.

Reference

1. S. U. Khan, M. Al-Shahry, W. B. Ingler, "Efficient photochemical water splitting by a chemically modified n-TiO2," Science **297**(5590), 2243-2245 (2002).
2. W.-J. Yin, H. Tang, S.-H. Wei, M. M. Al-Jassim, J. Turner, Y. Yan, "Band structure engineering of semiconductors for enhanced photoelectrochemical water splitting: the case of TiO 2," Phys. Rev. B: Condens. Matter **82**(4), 045106 (2010).
3. J. Nowotny, *Oxide semiconductors for solar energy conversion: titanium dioxide* (CRC Press, 2011).
4. C. Scales, P. Berini, "Thin-film schottky barrier photodetector models," IEEE Journal of quantum electronics **46**(5), 633-643 (2010).
5. M. L. Brongersma, N. J. Halas, P. Nordlander, "Plasmon-induced hot carrier science and technology," Nat. Nanotechnol. **10**(1), 25-34 (2015).
6. C. Clavero, "Plasmon-induced hot-electron generation at nanoparticle/metal-oxide interfaces for photovoltaic and photocatalytic devices," Nat. Photonics **8**(2), 95-103 (2014).
7. J. B. Chou, Y. X. Yeng, A. Lenert, V. Rinnerbauer, I. Celanovic, M. Soljačić, E. N. Wang, S.-G. Kim, "Design of wide-angle selective absorbers/emitters with dielectric filled metallic photonic crystals for energy applications," Opt. Express **22**(101), A144-A154 (2014).
8. J. B. Chou, Y. X. Yeng, Y. E. Lee, A. Lenert, V. Rinnerbauer, I. Celanovic, M. Soljačić, N. X. Fang, E. N. Wang, S. G. Kim, "Enabling ideal selective solar absorption with 2D metallic dielectric photonic crystals," Adv. Mater. **26**(47), 8041-8045 (2014).
9. J. B. Chou, X.-H. Li, Y. Wang, D. P. Fenning, A. Elfaer, J. Viegas, M. Jouiad, Y. Shao-Horn, S.-G. Kim, "Surface plasmon assisted hot electron collection in wafer-scale metallic-semiconductor photonic crystals," Opt. Express **24**(18), A1234-A1244 (2016).
10. P. Narang, R. Sundararaman, H. A. Atwater, "Plasmonic hot carrier dynamics in solid-state and chemical systems for energy conversion," Nanophotonics (2016).
11. R. H. Fowler, "The analysis of photoelectric sensitivity curves for clean metals at various temperatures," Phys. Rev. **38**(1), 45 (1931).
12. S. M. Sze, K. K. Ng, *Physics of semiconductor devices,* (John Wiley & Sons, 2006).
13. Z. Bian, T. Tachikawa, P. Zhang, M. Fujitsuka, T. Majima, "Au/TiO_2 superstructure-based plasmonic photocatalysts exhibiting efficient charge separation and unprecedented activity," J. Am. Chem. Soc. **136**(1), 458-465 (2013).
14. K. Wu, J. Chen, J. McBride, T. Lian, "Efficient hot-electron transfer by a plasmon-induced interfacial charge-transfer transition," Science **349**(6248), 632-635 (2015).
15. Y. Nishijima, K. Ueno, Y. Yokota, K. Murakoshi, H. Misawa, "Plasmon-assisted photocurrent generation from visible to near-infrared wavelength using a Au-nanorods/TiO_2 electrode," J. Phys. Chem. Lett. **1**(13), 2031-2036 (2010).
16. Y. K. Lee, C. H. Jung, J. Park, H. Seo, G. A. Somorjai, J. Y. Park, "Surface plasmon-driven hot electron flow probed with metal-semiconductor nanodiodes," Nano Lett. **11**(10), 4251-4255 (2011).

17. E. D. Palik, *Handbook of optical constants of solids,* (Academic Press, 1998).
18. A. M. Brown, R. Sundararaman, P. Narang, W. A. Goddard III, H. A. Atwater, "Non-Radiative Plasmon Decay and Hot Carrier Dynamics: Effects of Phonons, Surfaces and Geometry," ACS nano **10**, 957-966 (2015).
19. Y. Wang, "Study on the photoelectric hot electrons generation and transport with metallic-semiconductor photonic crystals," Massachusetts Institute of Technology, (2015).
20. F. P. García de Arquer, A. Mihi, D. Kufer, G. Konstantatos, "Photoelectric energy conversion of plasmon-generated hot carriers in metal–insulator–semiconductor structures," ACS nano **7**(4), 3581-3588 (2013).
21. S. A. Maier, *Plasmonics: fundamentals and applications* (Springer Science & Business Media, 2007).
22. J. Pitarke, V. Silkin, E. Chulkov, P. Echenique, "Theory of surface plasmons and surface-plasmon polaritons," Reports on Progress in Physics **70**(1), 1 (2006).
23. A. Liebsch, *Electronic excitations at metal surfaces,* (Springer Science & Business Media, 2013).
24. J. B. Khurgin, "How to deal with the loss in plasmonics and metamaterials," Nat. Nanotechnol. **10**(1), 2-6 (2015).
25. W. Li, J. G. Valentine, "Harvesting the loss: surface plasmon-based hot electron photodetection," Nanophotonics **6**(1), 177-191 (2017).
26. S. V. Boriskina, H. Ghasemi, G. Chen, "Plasmonic materials for energy: From physics to applications," Mater. Today **16**(10), 375-386 (2013).
27. E. Hutter, J. H. Fendler, "Exploitation of localized surface plasmon resonance," Adv. Mater. **16**(19), 1685-1706 (2004).
28. H. Chen, L. Shao, Q. Li, J. Wang, "Gold nanorods and their plasmonic properties," Chem. Soci. Rev. **42**(7), 2679-2724 (2013).
29. L. J. Sherry, S.-H. Chang, G. C. Schatz, R. P. Van Duyne, B. J. Wiley, Y. Xia, "Localized surface plasmon resonance spectroscopy of single silver nanocubes," Nano Lett. **5**(10), 2034-2038 (2005).
30. J. Henzie, J. Lee, M. H. Lee, W. Hasan, T. W. Odom, "Nanofabrication of plasmonic structures," Annu. Rev. Phy. Chem. **60**, 147-165 (2009).
31. J. Li, S. K. Cushing, F. Meng, T. R. Senty, A. D. Bristow, N. Wu, "Plasmon-induced resonance energy transfer for solar energy conversion," Nat. Photonics **9**(9), 601-607 (2015).
32. S. Mubeen, J. Lee, N. Singh, S. Krämer, G. D. Stucky, M. Moskovits, "An autonomous photosynthetic device in which all charge carriers derive from surface plasmons," Nat. Nanotechnol. **8**(4), 247-251 (2013).
33. F. P. García de Arquer, A. Mihi, G. Konstantatos, "Large area plasmonic crystal hot electron based photodetectors," ACS Photonics **2**(7), 950-957 (2015).
34. T. P. White, K. R. Catchpole, "Plasmon-enhanced internal photoemission for photovoltaics: theoretical efficiency limits," Appl. Phys. Lett. **101**(7), 073905 (2012).

35. A. J. Leenheer, P. Narang, N. S. Lewis, H. A. Atwater, "Solar energy conversion via hot electron internal photoemission in metallic nanostructures: Efficiency estimates," J. Appl. Phys. **115**(13), 134301 (2014).
36. A. O. Govorov, H. Zhang, Y. K. Gun'ko, "Theory of photoinjection of hot plasmonic carriers from metal nanostructures into semiconductors and surface molecules," J. Phys. Chem. C **117**(32), 16616-16631 (2013).
37. J. A. Schuller, E. S. Barnard, W. Cai, Y. C. Jun, J. S. White, M. L. Brongersma, "Plasmonics for extreme light concentration and manipulation," Nat. Mater. **9**(3), 193-204 (2010).
38. R. Sundararaman, P. Narang, A. S. Jermyn, W. A. Goddard III, H. A. Atwater, "Theoretical predictions for hot-carrier generation from surface plasmon decay," Nat. Commun. **5**, 5788 (2014).
39. M. Bernardi, J. Mustafa, J. B. Neaton, S. G. Louie, "Theory and computation of hot carriers generated by surface plasmon polaritons in noble metals," Nat. Commun. **6**, 7044 (2015).
40. E. Fermi, *Nuclear physics: a course given by Enrico Fermi at the University of Chicago,* (University of Chicago Press, 1950).
41. A. Manjavacas, J. G. Liu, V. Kulkarni, P. Nordlander, "Plasmon-induced hot carriers in metallic nanoparticles," ACS nano **8**(8), 7630-7638 (2014).
42. C. S. Kumarasinghe, M. Premaratne, Q. Bao, G. P. Agrawal, "Theoretical analysis of hot electron dynamics in nanorods," Scientific reports **5**, 12140 (2015).
43. H. Kanter, "Slow-electron mean free paths in aluminum, silver, and gold," Phys. Rev. B: Condens. Matter **1**(2), 522 (1970).
44. G. V. Hartland, "Optical studies of dynamics in noble metal nanostructures," Chem. Rev. **111**(6), 3858-3887 (2011).
45. H. Harutyunyan, A. B. Martinson, D. Rosenmann, L. K. Khorashad, L. V. Besteiro, A. O. Govorov, G. P. Wiederrecht, "Anomalous ultrafast dynamics of hot plasmonic electrons in nanostructures with hot spots," Nat. Nanotechnol. **10**(9), 770-774 (2015).
46. B. Y. Zheng, H. Zhao, A. Manjavacas, M. McClain, P. Nordlander, N. J. Halas, "Distinguishing between plasmon-induced and photoexcited carriers in a device geometry," Nat. Commun. **6,** 7797 (2015).
47. Q. Y. Chen, C. W. Bates Jr, "Geometrical factors in enhanced photoyield from small metal particles," Phys. Rev. Lett. **57**(21), 2737 (1986).
48. H. Chalabi, D. Schoen, M. L. Brongersma, "Hot-electron photodetection with a plasmonic nanostripe antenna," Nano Lett. **14**(3), 1374-1380 (2014).
49. C. Cercignani, "The Boltzmann equation," in *The Boltzmann Equation and Its Applications*, (Springer, 1988).
50. S. V. Boriskina, J. Zhou, W.-C. Hsu, B. Liao, G. Chen, "Limiting efficiencies of solar energy conversion and photo-detection via internal emission of hot electrons and hot holes in gold," SPIE, 960816-960816-960817, (2015).

51. W. Li, Z. J. Coppens, L. V. Besteiro, W. Wang, A. O. Govorov, J. Valentine, "Circularly polarized light detection with hot electrons in chiral plasmonic metamaterials," Nat. Commun. **6** 8379 (2015).
52. M. W. Knight, Y. Wang, A. S. Urban, A. Sobhani, B. Y. Zheng, P. Nordlander, N. J. Halas, "Embedding plasmonic nanostructure diodes enhances hot electron emission," Nano Lett. **13**(4), 1687-1692 (2013).
53. J. Lee, S. Mubeen, X. Ji, G. D. Stucky, M. Moskovits, "Plasmonic photoanodes for solar water splitting with visible light," Nano Lett. **12**(9), 5014-5019 (2012).
54. D. Jin, Q. Hu, D. Neuhauser, F. von Cube, Y. Yang, R. Sachan, T. S. Luk, D. C. Bell, N. X. Fang, "Quantum-spillover-enhanced surface-plasmonic absorption at the interface of silver and high-index dielectrics," Phys. Rev. Lett. **115**(19), 193901 (2015).
55. J. D. Jackson, *Electrodynamics,* (Wiley Online Library, 1975).
56. G. R. Werner, C. A. Bauer, J. R. Cary, "A more accurate, stable, FDTD algorithm for electromagnetics in anisotropic dielectrics," J. Comput. Phys. **255**(436-455 (2013).
57. Z. Yang, Q. Li, F. Ruan, Z. Li, B. Ren, H. Xu, Z. Tian, "FDTD for plasmonics: Applications in enhanced Raman spectroscopy," Chinese Science Bulletin **55**(24), 2635-2642 (2010).
58. E. Lorenzo, *Solar electricity: engineering of photovoltaic systems,* (Earthscan/James & James, 1994).
59. P. Pillai, A. Corpus Mendoza, M. De Souza, G. Bree, D. Jeng, "Extraction of Schottky barrier at the F-doped SnO2/TiO2 interface in Dye Sensitized solar cells," J. Renew. Sustain. Energy **6**(1), 013142 (2014).
60. F. P. García de Arquer, "Plasmonic hot-carrier optoelectronics," The Institute of Photonic Sciences, Barcelona, (2015).
61. T. Kelf, Y. Sugawara, R. Cole, J. Baumberg, M. Abdelsalam, S. Cintra, S. Mahajan, A. Russell, P. Bartlett, "Localized and delocalized plasmons in metallic nanovoids," Phys. Rev. B: Condens. Matter **74**(24), 245415 (2006).
62. N. M. Perney, J. J. Baumberg, M. E. Zoorob, M. D. Charlton, S. Mahnkopf, C. M. Netti, "Tuning localized plasmons in nanostructured substrates for surface-enhanced Raman scattering," Opt. Express **14**(2), 847-857 (2006).
63. P. B. Johnson, R.-W. Christy, "Optical constants of the noble metals," Phys. Rev. B: Condens. Matter **6**(12), 4370 (1972).
64. N. S Rajput, S.-H. Yang, X.-H. Li, S.-G. Kim, M. Jouiad, "Investigation of plasmonic resonance in metal/dielectric nanocavities for high efficiency water splitting device," Energy & Environmental Science, Under Review, (2017).
65. X.-H. Li, J. B. Chou, W. L. Kwan, A. M. Elsharif, S.-G. Kim, "Effect of anisotropic electron momentum distribution of surface plasmon on internal photoemission of a Schottky hot carrier device," Opt. Express **25**(8), A264-A273 (2017).
66. M. Fox, *Optical properties of solids,* (AAPT, 2002).
67. C. Berglund, W. Spicer, "Photoemission studies of copper and silver: experiment," Phys. Rev. **136**(4A), A1044 (1964).

68. R. S. Ikhsanov, V. E. e. Babicheva, I. E. e. Protsenko, A. V. e. Uskov, M. E. e. Guzhva, "Bulk photoemission from metal films and nanoparticles," Quant. Electron. **45**(1), 50 (2015).